JCI The Journal of Clinical Investigation

A CD138+ tumor-associated macrophage-Siglec-F+ neutrophil feedforward loop promotes immune evasion in pancreatic cancer

Chao Wang, Qi Zhang, Jinyan Huang, Fangyu Lin, Danyang Zhao, Youling Mu, Junshuo Tong, Jinping Li, Yingjiqiong Liang, Tao Zeng, Fukang Shi, Hang Shen, Tingting Lu, Tingbo Liang

J Clin Invest. 2026. https://doi.org/10.1172/JCI199516.

Research In-Press Preview Gastroenterology Immunology Oncology

Graphical abstract

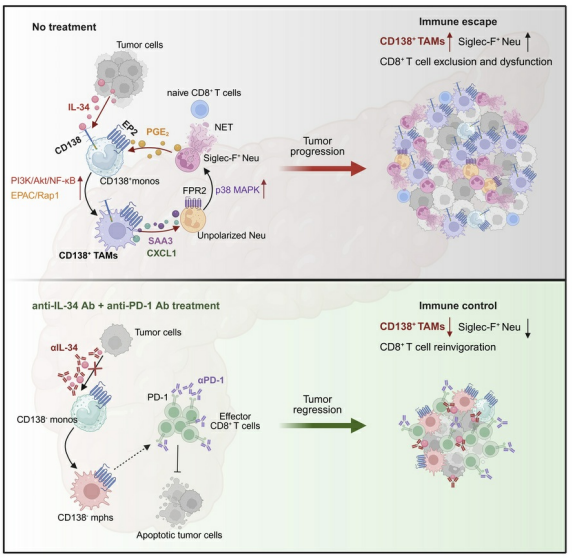

A CD138$^+$ tumor-associated macrophage-Siglec-F$^+$ neutrophil feedforward loop promotes immune evasion in pancreatic cancer

Chao Wang[1,2,3], Qi Zhang[1,2,3,4,5,6], Jinyan Huang[1], Fangyu Lin[1,2], Danyang Zhao[1], Youling Mu[1], Junshuo Tong[1], Jinping Li[1], Yingjiqiong Liang[1], Tao Zeng[1], Fukang Shi[1,2], Hang Shen[1,2], Tingting Lu[7], Tingbo Liang[1,2,3,4,5,6]

[1]Zhejiang Provincial Key Laboratory of Pancreatic Disease, [2]Department of Hepatobiliary and Pancreatic Surgery, and [3]MOE Joint International Research Laboratory of Pancreatic Diseases, the First Affiliated Hospital, Zhejiang University School of Medicine; Hangzhou, China. [4]Zhejiang Clinical Research Center of Hepatobiliary and Pancreatic Diseases; Hangzhou, China. [5]The Innovation Center for the Study of Pancreatic Diseases of Zhejiang Province; Hangzhou, China. [6]Zhejiang University Cancer Center; Hangzhou, China. [7]Bio-X Institutes, Key Laboratory for the Genetics of Developmental and Neuropsychiatric Disorders (Ministry of Education), Shanghai Jiao Tong University; Shanghai, China.

Address correspondence to: Tingbo Liang or Chao Wang, Teaching and Research Center of the First College of Zhejiang University, No.17, Laozheda Straight Road, Xiaoying Street, Shangcheng District, Hangzhou, Zhejiang Province, China. Phone: 86-0571-87236601; E-mail: liangtingbo@zju.edu.cn (TL). E-mail: chaowang2019@zju.edu.cn (CW).

Authorship note: CW, QZ, and JH contributed equally to this work.

Conflict of interest: The authors have declared that no conflict of interest exists.

Abstract

Immune evasion is a major obstacle ahead of pancreatic cancer therapy. Recent data implicate pro-inflammatory macrophages in the progression of pancreatic ductal adenocarcinoma (PDAC) and its therapeutic response. However, whether or which of the pro-inflammatory macrophage subtypes play a crucial role in the immune escape of PDAC remains unclear. Here we identify a population of $CD138^+$ tumor-associated macrophages (TAMs), characterized by their pro-inflammatory and neutrophil-chemotactic activity, which undergo significant expansion in both PDAC patients and mouse models. These cells are elicited by a local synergy between IL-34-syndecan-1 and PGE_2-EP2 signaling and are associated with immune evasion and poor clinical outcomes in patients, while also promoting immune escape and disease progression in mouse models. Mechanistically, $CD138^+$ TAMs establish a feedforward loop with immunosuppressive Siglec-F^+ neutrophils, which exhibit elevated PGE_2 expression, via the secretion of SAA3 and CXCL1. Targeting $CD138^+$ TAMs by disrupting IL-34-syndecan-1 signaling with anti-IL-34 neutralizing antibodies significantly suppresses PDAC progression, especially when combined with anti-PD-1 antibodies. Together, our study elucidates a $CD138^+$ TAM-Siglec-F^+ neutrophil axis that drives immune escape in PDAC and proposes a therapeutic strategy that integrates IL-34-syndecan-1 signaling blockade with anti-PD-1 immunotherapy for the treatment of PDAC.

Graphical abstract

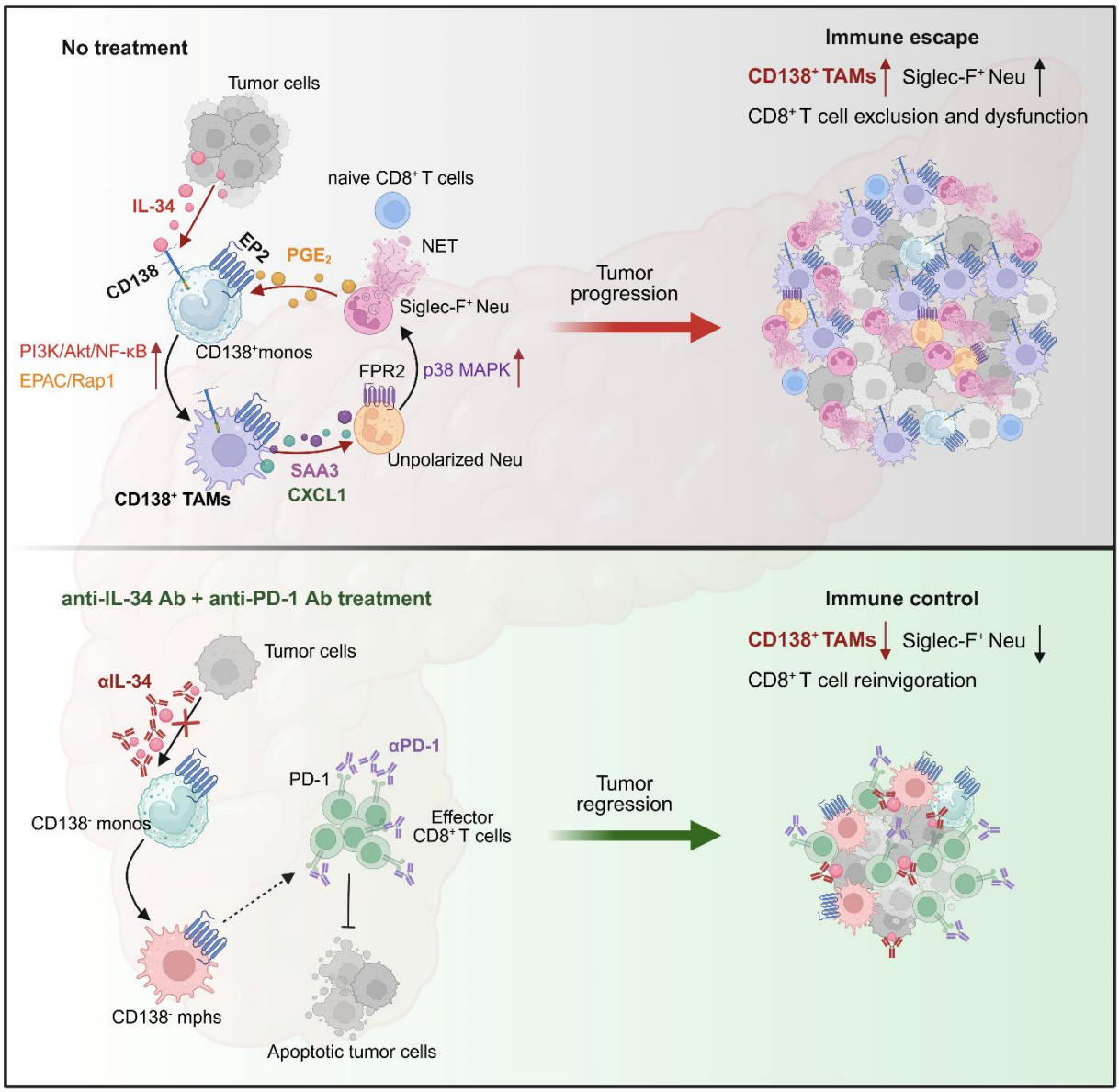

Main Text

Introduction

Pancreatic cancer, predominantly pancreatic ductal adenocarcinoma (PDAC), is recognized as one of the most aggressive solid malignancies, exhibiting nearly uniform mortality rates and ranking as the third leading cause of cancer-related deaths in the United States(1). PDAC is notoriously resistant to current therapies, including immunotherapy, primarily due to its immunosuppressive tumor microenvironment (TME)(2). Tumor-associated macrophages (TAMs), which are abundant within the PDAC TME, are believed to significantly influence tumor immune evasion(3), although it remains undefined which TAM subset plays a pivotal role. Traditionally, pro-inflammatory macrophages have been regarded as anti-tumorigenic, characterized by an M1-like phenotype(4). Nonetheless, these macrophages harbor considerable heterogeneity and functional plasticity during disease progression and therapy(5). IL-1β^+ TAMs trigger pathogenic inflammation, fueling PDAC development(6). Inflammatory macrophage-derived granulin and CXCL3 facilitate the generation of myofibroblasts, thereby driving tumor metastasis(7, 8). Conversely, upon exposure to radiotherapy, targeted therapy, and/or immunotherapy, the pro-inflammatory polarization of macrophages plays a crucial role in reactivating anti-tumor immunity(9–11). However, whether or which of the pro-inflammatory macrophage subtypes play a crucial role during the immune evasion of PDAC is still unclear, as does the manner in which local signals elicit their functions.

Previous studies have reported interactions between TAMs and neutrophils within the TME across several cancer types(12, 13). Mesothelin secretion by metastatic pancreatic cancer cells induces the expression of S100A9 in macrophages, which leads to increased neutrophil infiltration into the lungs and the formation of neutrophil extracellular traps (NETs), thereby supporting tumor

metastasis(14). Furthermore, dual targeting of $CCR2^+$ TAMs and $CXCR2^+$ neutrophils improves anti-tumor immunity compared to either strategy alone, indicating a compensatory response from the alternative myeloid subset(15). However, the interactions between TAMs and neutrophils within the primary tumor of PDAC and their roles in tumor immune evasion remain unclear. A better understanding of these interactions is needed to facilitate the rational targeting of TAMs to overcome immune evasion in PDAC.

IL-34, a short-chain helical hematopoietic cytokine, plays a crucial role in regulating the differentiation, proliferation, and survival of myeloid cells(16, 17). It is increasingly evident that IL-34 significantly influences the immune escape and progression of several cancer types by inducing M2 polarization of TAMs(17, 18). Despite this, the specific roles of IL-34 in PDAC remain poorly understood. Syndecan-1, also known as CD138, serves as a functional receptor for IL-34; upon engagement, it stimulates the migration of myeloid cells and modulates the activation of CSF1R(19). Recent research has revealed that syndecan-1 localized on the surface of pancreatic cancer cells regulates macropinocytosis, an essential metabolic pathway that supports tumor growth(20). Nevertheless, the regulatory effects of IL-34-syndecan-1 signaling on the phenotype and function of myeloid cells within the TME, as well as the impact of this process on tumor immune evasion are still undefined.

In this study, we delved into the influence of TAMs on the immune escape of PDAC, uncovering the expansion of a population of $CD138^+$ TAMs in both PDAC patients and mouse models. This unique subset of TAMs exhibited pro-inflammatory and neutrophil-chemotactic activity. Their generation was collaboratively driven by IL-34-syndecan-1 and PGE_2-EP2 signaling, establishing a feedforward loop with immunosuppressive PGE_2-expressing Siglec-F^+ neutrophils through the secretion of SAA3 and CXCL1, thereby contributing to tumor immune evasion. Notably, we

demonstrated that targeting CD138$^+$ TAMs via the blockade of IL-34-syndecan-1 signaling effectively impeded PDAC progression, particularly when combined with anti-PD-1 antibodies. Our findings underscore the crucial roles of CD138$^+$ TAMs in facilitating tumor immune evasion and provide valuable insights for developing combination therapy strategies that target these cells in conjunction with anti-PD-1 immunotherapy for the effective treatment of PDAC.

Results

A CD138$^+$ TAM subset is identified and associated with immune evasion and poor outcomes in PDAC

To explore the impact of tumor-infiltrating macrophages on immune evasion in PDAC, we assessed the cellular composition of the TME using multiplex immunohistochemistry (mIHC) staining on a tissue array comprising 41 paired adjacent benign and tumor tissues from PDAC patients (referred to as Cohort 2) (Supplemental Figure 1, A and B). The results revealed a significant decrease in the abundance of CD8$^+$ T cells, accompanied by an increase in the density of natural killer (NK) cells, plasma cells, macrophages, neutrophils, and dendritic cells (DCs) in tumor tissues compared to adjacent benign tissues (Figure 1A). Furthermore, the analysis of T cell status within the PDAC TME indicated that the proportions of activated CD8$^+$ cytotoxic T cells were significantly reduced, while the frequencies of exhausted CD8$^+$ T cells and regulatory T (Treg) cells were markedly elevated (Figure 1B). These findings suggest the presence of an immunosuppressive TME in PDAC patients.

Notably, we identified a subset of TAMs expressing CD138, which was found to be expanded in the tumor tissues of PDAC patients in Cohort 2 (Figure 1C and Supplemental Figure 1B). The emergence of this subset was further validated in fresh samples from PDAC patients, including

adjacent benign tissues (n=58) and tumor tissues (n=103), collectively referred to as Cohort 1, utilizing flow cytometry (Figure 1, D-F). Thus, we investigated the roles of $CD138^+$ TAMs in tumor immune escape. The findings demonstrated a negative correlation between the abundance of $CD138^+$ TAMs and the presence of both $CD8^+$ T cells and activated cytotoxic $CD8^+$ T cells, while exhibiting a positive association with tumor cell density (Figure 1G). However, this abundance showed no significant relationship with the density of Treg cells or exhausted $CD8^+$ T cells (Supplemental Figure 1C). These findings suggest that $CD138^+$ TAMs contribute to tumor immune evasion by promoting the exclusion and dysfunction of $CD8^+$ T cells. To further explore the impact of $CD138^+$ TAMs on PDAC progression, we assessed their abundance in a tissue array comprising tumor samples from 114 patients with available prognostic information (designated as Cohort 3) using mIHC staining. Patients were categorized into two subgroups: $CD138^+$ TAM-low (n=63) and $CD138^+$ TAM-high (n=51), based on the density of $CD138^+$ TAMs (Figure 1H and Supplemental Figure 1D). Kaplan-Meier survival analysis demonstrated that patients in the $CD138^+$ TAM-high group experienced significantly shorter overall survival times compared to those in the $CD138^+$ TAM-low group (p-value=0.0069, Figure 1H). Additionally, univariate analysis revealed a negative correlation between $CD138^+$ TAM abundance and tumor differentiation (Supplemental Table 1), indicating that patients with elevated levels of $CD138^+$ TAMs are more likely to exhibit aggressive tumor behavior. Therefore, $CD138^+$ TAMs may serve as potential indicators for PDAC progression.

To confirm the presence of $CD138^+$ TAMs in PDAC mouse models, we first established a spontaneous PDAC mouse model using $Kras^{G12D/+}Trp53^{R172H/+}Pdx1^{cre/+}$ (hereafter referred to as KPC) mice(21). Tumor samples were collected at the stage when the disease burden in KPC mice became evident. As expected, a significant number of $CD138^+$ TAMs were identified in the tumor

tissues of KPC mice (Figure 1, I-L). These observations were further corroborated in the orthotopic KPC mouse model (Supplemental Figure 1, E-H) and in another spontaneous PDAC mouse model, *Kras*$^{LSL\text{-}G12D}$*TgfβR2*$^{flox/flox}$*Ptf1a*$^{cre/+}$ (hereafter referred to as KTC) mice(22) (Supplemental Figure 1, I-L). Collectively, these findings indicate that CD138$^+$ TAMs are expanded in the PDAC TME and may contribute to tumor progression by promoting immune evasion.

CD138$^+$ TAMs exhibit robust pro-inflammatory and neutrophil-chemotactic activity

Previous studies have documented the emergence of an anti-inflammatory population of CD138$^+$ macrophages during the resolution of lupus(23), infectious diseases(24), and the progression of abdominal aortic aneurysm(25). These cells are characterized by the elevated expression levels of IL-10R, CD206, and CCR2, as well as the activation of the cAMP/PKA/CREB pathway. This prompted us to investigate whether CD138$^+$ TAMs within the PDAC TME represent such anti-inflammatory populations. We conducted a transcriptional comparison between CD138$^+$ and CD138$^-$ TAMs in orthotopic tumors using Smart-seq. Contrary to our expectations, the transcriptional profile of CD138$^+$ TAMs did not exhibit up-regulation of *Il10ra*, *Il10rb*, *Mrc1*, or *Ccr2*, nor did it demonstrate enrichment in the cAMP signaling pathway (Supplemental Figure 2, A and B). This may be attributed to the high expression of the cAMP-hydrolyzing enzyme phosphodiesterase 4D (*Pde4d*)(26) in these cells (Supplemental Figure 3F). Flow cytometric results confirmed the low expression levels of IL-10R and CD206 in CD138$^+$ TAMs from patients with PDAC (Supplemental Figure 2C). These findings suggest that CD138$^+$ TAMs may constitute a subset of macrophages separated from the previously identified anti-inflammatory population.

To further investigate the phenotype of CD138$^+$ TAMs within the PDAC TME, single-cell RNA sequencing (scRNA-seq) was performed on F4/80$^+$ cells sorted from tumor tissues of the

orthotopic KPC model. Following quality control, we extracted and analyzed a total of 11,711 cells from ten mice. Genes were identified and embedded in a non-discriminative manner, with dimensionality reduction executed using uniform manifold approximation and projection (UMAP). Seven clusters were identified and categorized into six macrophage subclusters, along with one dendritic cell (DC) subcluster, which was distinguished by the up-regulation of the classical DC marker, *Flt3* (Figure 2, A and B). Among the macrophage subclusters, MM2 exhibited elevated expression of *Cxcl9* and *Stat1*, indicative of an 'M1 (hot)' phenotype(27). MM6 was characterized by high expression levels of pro-inflammatory genes (*Il1b* and *Clec4e*) and aligned with inflammatory and non-cytotoxic IL-1β^+ macrophages(28). Additionally, a subcluster (MM3) was identified as a transitional population between monocytes and macrophages, retaining monocyte markers such as *Plac8* and *Ly6c2*(29). Other TAM clusters expressed genes linked to cell cycle regulation (*Ube2c*, *Top2a*, and *Mki67* in MM4) or an M2-like phenotype (*Mrc1*, *Pdgfc*, and *Wwp1* in MM5)(30, 31). Our analysis revealed a subcluster (MM1) with high expression levels of *Sdc1*, the gene encoding CD138 (Figure 2, A and B). A publicly available scRNA-seq dataset from the pancreas of healthy mice and those with acute pancreatitis(32) was integrated with our data to compare the proportions of macrophage subsets (Supplemental Figure 3, A-C). We observed that the frequency of *Sdc1*$^+$ macrophages exhibited the most marked increase among all macrophage subsets within tumor tissues (Supplemental Figure 3D). Furthermore, gene signature scores for these macrophage subsets were computed from a bulk RNA-seq dataset of PDAC patients sourced from The Cancer Genome Atlas (TCGA), utilizing the marker genes identified in the scRNA-seq data. Patients were categorized into two groups based on their gene signature score levels. Survival analysis indicated that patients in the MM1 score-high group experienced significantly shorter overall survival times (Supplemental Figure 3E). These findings suggest that *Sdc1*$^+$ macrophages

may play a critical role in promoting the progression of pancreatic cancer. Consequently, we conducted Gene Set Enrichment Analysis (GSEA) for *Sdc1*$^+$ macrophages. The results indicated that the transcriptome of this population was enriched in neutrophil chemotaxis (*Cxcl1*, *Ccl2*, and *Cxcl3*), positive regulation of secretion (*Sdc1*, *Tlr4*, and *Anxa2*), acute phase response (*Saa3*, *Fn1*, and *Ednrb*), and cellular response to hypoxia (*Egln3*, *Ak4*, and *Pgk1*), while being depleted of pathways related to the regulation of NK cell-mediated immunity, antigen presentation, and complement activation, as determined by Gene Ontology (GO) terms (Figure 2, C and D). Smart-seq data revealed a comparable gene signature in CD138$^+$ macrophages isolated from orthotopic tumors, characterized by the up-regulation of pro-inflammatory and neutrophil-chemotactic factors, including *Saa3* and *Cxcl1* (Supplemental Figure 3F). Flow cytometry and mIHC analysis confirmed a marked elevation of SAA3 (SAA1, the ortholog of murine SAA3(33)) and CXCL1 in CD138$^+$ TAMs derived from tumor tissues of PDAC patients and orthotopic mouse models (Figure 2, E-G). These findings underscore CD138$^+$ TAMs as a unique subset of macrophages characterized by the expression of pro-inflammatory and neutrophil-chemotactic programs within the PDAC TME.

IL-34 and PGE_2 elicit CD138$^+$ TAMs

To explore the mechanisms responsible for the generation of CD138$^+$ TAMs, we established a CD45.1/CD45.2 chimera model with orthotopic KPC tumors (Supplemental Figure 4A). Flow cytometry analysis revealed that CD138$^+$ TAMs in the chimeric mice predominantly expressed CD45.1 (Supplemental Figure 4, B and C), indicating that these cells originate from circulating monocytes rather than from tissue-resident macrophages. Given that syndecan-1 serves as a functional receptor for IL-34(34), we investigated the potential roles of IL-34 in eliciting the

CD138$^+$ TAM state. To determine the expression of IL-34 in PDAC, scRNA-seq was conducted using tumor tissues isolated from orthotopic KPC mice 21 days post-implantation. The data were then integrated with a publicly available scRNA-seq dataset from blood samples of three orthotopic KPC mice(6). Following quality control, we extracted and reanalyzed a total of 22,061 cells. Genes were identified and embedded in a non-discriminative manner, with dimensionality reduction performed using UMAP. Eight clusters were identified and categorized into two non-immune cell types: ductal cells and cancer-associated fibroblasts (CAFs), as well as six immune cell types: monocytes/macrophages, neutrophils, DCs (including cDC1 and cDC2), B cells, T/NK cells, and mast cells (Supplemental Figure 5A). Signature genes for each cluster were cross-referenced with established markers from the literature to accurately identify the different cell types represented by the clusters (Supplemental Figure 5B). The results revealed that IL-34 was predominantly derived from ductal cells (Supplemental Figure 5C). mIHC analysis confirmed a substantial increase in IL-34 levels in tumor cells from both orthotopic KPC mice and patients with PDAC (Supplemental Figure 5, D-G). However, treatment of mouse bone marrow-derived macrophages (BMDMs) with IL-34 did not induce syndecan-1 expression or the synthesis of SAA3 and CXCL1, suggesting the requirement of additional factors (Figure 3, A-C). Prostaglandin E2 (PGE_2), a lipid inflammatory mediator, was found to be elevated in PDAC(35–37), stimulating syndecan-1 expression in BMDMs(24). Furthermore, our findings indicated a notable rise in PGE_2 levels in the serum of both orthotopic KPC mice and individuals with PDAC (Supplemental Figure 6, A and B). RT-PCR data revealed elevated expression levels of *Ptgs2* (COX-2, a critical enzyme in PGE_2 synthesis(38)) in neutrophils isolated from orthotopic KPC tumors 10 days post-implantation (Supplemental Figure 6C), suggesting that PGE_2 is primarily derived from tumor-infiltrating neutrophils prior to the emergence of CD138$^+$ TAMs (Supplemental Figure 15). Thus,

we investigated whether PGE_2 contributed to the production of $CD138^+$ TAMs. Flow cytometric analysis demonstrated that PGE_2 alone up-regulated the expression of syndecan-1 in a dose-dependent manner, while exhibiting limited effects on the synthesis of SAA3 and CXCL1 in BMDMs (Figure 3, A-C and Supplemental Figure 6, D and E). However, its co-treatment with IL-34 resulted in a robust production of SAA3 and CXCL1 in BMDMs (Figure 3, A-C). Bulk RNA-seq revealed a distinct set of transcripts that were synergistically induced by IL-34 plus PGE_2 (Figure 3D). These transcripts were notably enriched in the transcriptome of *Sdc1*$^+$ TAMs and among the driver genes of the monocyte-to-*Sdc1*$^+$ TAM transition, as evidenced by scRNA-seq data, which included reclustering of the monocyte/macrophage subset (Figure 3E and Supplemental Figure 7, A-D). These genes encoded for proteins that trigger acute inflammation (*Saa3*) and enhance neutrophil recruitment (*Cxcl1*, *Ccl2*, and *Cxcl3*) (Figure 3D). Furthermore, the morphology, migration, and phagocytosis of $CD138^+$ macrophages induced by the combination of IL-34 and PGE_2, along with $CD138^+$ TAMs isolated from orthotopic tumors, were analyzed. We found that both of them showed enlarged size, irregular shape, extended pseudopods, and enhanced migration and phagocytic capabilities compared to the control group (Supplemental Figure 8). Together, these findings suggest that IL-34 and PGE_2 induce the production of $CD138^+$ TAMs.

To further confirm this hypothesis, we examined the effects of IL-34 and PGE_2 on the differentiation of $CD138^+$ TAMs in vivo. RT-PCR analysis revealed a dramatic increase in the transcriptional levels of EP2 (encoded by *Ptger2*) rather than other PGE_2 receptors(39) in both $CD138^+$ TAMs isolated from orthotopic tumors and BMDMs exposed to PGE_2 (Supplemental Figure 7, E and F). Furthermore, the introduction of PGE_2 receptor inhibitors into the BMDM cultures demonstrated that the EP2 antagonist (PF-04418948) notably inhibited the effect of PGE_2 on the up-regulation of syndecan-1 expression (Supplemental Figure 7, G and H). Thus, we

established an orthotopic model comprising *Ptger2*$^{flox/flox}$; *Csf1r-Cre* (hereafter referred to as Ptger2-cKO) mice and a KPC cell line with silenced IL-34 expression, which was subsequently analyzed using flow cytometry (Supplemental Figure 7, I-K). The results indicated that either silencing IL-34 expression or conditionally knocking-out of *Ptger2* in monocytes/macrophages effectively impeded the generation of CD138$^+$ TAMs in the orthotopic tumors (Figure 3, F-H). To determine whether IL-34 relies on syndecan-1 for mediating CD138$^+$ TAM differentiation, BMDMs derived from *Sdc1*$^{flox/flox}$; *Csf1r-Cre* (hereafter referred to as Sdc1-cKO) mice, which allow for the conditional knockout of *Sdc1* in monocytes/macrophages, were exposed to IL-34 and PGE_2. Flow cytometric analysis showed that the knockout of *Sdc1* in BMDMs significantly suppressed their synthesis of SAA3 and CXCL1 (Figure 3, I and J). The introduction of Synstatin, a selective inhibitor of syndecan-1(40), into the BMDM culture system yielded similar results (Figure 3, K and L). Collectively, these phenomena demonstrate that CD138$^+$ TAMs are induced by IL-34-Syndecan-1 and PGE_2-EP2 signaling.

Next, we investigate the molecular mechanisms through which IL-34 and PGE_2 drive the differentiation of CD138$^+$ TAMs. Notably, we observed an up-regulated gene set enriched in the PI3K-Akt, NF-kappa B, and Rap1 signaling pathways in *Sdc1*$^+$ TAMs (Supplemental Figure 9A). These pathways are well-established downstream signaling routes for CSF1R (a classical IL-34 receptor) and PGE_2 receptors(41, 42). Upon introducing antagonists or inhibitors targeting these pathways into the culture systems, we found that inhibitors of the PI3K-Akt (PI3K/AKT-IN-1) and NFκB (JSH-23) pathways suppressed the synthesis of SAA3 and CXCL1, while leaving CD138 expression unaffected in BMDMs cultured with IL-34 and PGE_2 (Supplemental Figure 9, B-D). In contrast, the EPAC/Rap1 pathway antagonist, ESI-08, significantly inhibited the expression of CD138, as well as the production of SAA3 and CXCL1 (Supplemental Figure 9, B-

D). These findings indicate that IL-34 activates the PI3K/Akt/NFκB pathway, while PGE_2 primarily stimulates the EPAC/Rap1 pathway, collectively driving the differentiation of $CD138^+$ TAMs. Together, these findings demonstrate that IL-34 and PGE_2 collaboratively induce the generation of $CD138^+$ TAMs within the PDAC TME and enhance the synthesis of pro-inflammatory factors such as SAA3 and CXCL1 in these cells.

$CD138^+$ TAMs promote the progression of PDAC by facilitating tumor immune escape

To investigate the roles of $CD138^+$ TAMs in the progression of PDAC, an adoptive transfer assay was conducted using the orthotopic KPC model. Briefly, $CD138^+$ TAMs extracted from orthotopic tumors were intravenously injected into orthotopic KPC mice every 3 to 4 days for a total of three injections, starting at 10 days post-tumor implantation (Figure 4A). The infiltration of $CD138^+$ TAMs into the TME was confirmed through flow cytometry (Supplemental Figure 10A). The results indicated that mice receiving the adoptive transfer of $CD138^+$ TAMs exhibited increased tumor weight and enhanced cell proliferation in tumor tissues, suggesting a more aggressive cancer phenotype compared to the control groups (Figure 4, B and C and Supplemental Figure 10, B and C). Notably, survival analysis revealed significantly shorter overall survival times in the group injected with $CD138^+$ TAMs (Figure 4D). Flow cytometric analysis revealed a marked reduction in the infiltration of $CD8^+$ T cells in mice following the adoptive transfer of $CD138^+$ TAMs (Figure 4E). scRNA-seq data indicated an increased proportion of $CD8^+$ T cells exhibiting a naïve phenotype, accompanied by a decrease in the fractions of effector-memory (T_{EM}), precursor-exhausted (Tpex), intermediate-exhausted (intermediate Tex), terminally-exhausted (Tex), and proliferating subsets within tumors that received the adoptive transfer of $CD138^+$ TAMs (Figure 4F and Supplemental Figure 10D). Furthermore, $CD8^+$ T cells in tumors injected with $CD138^+$

TAMs showed diminished activity and cytotoxicity, as evidenced by the reduced expression of effector factors (*Ifng*, *Gzmb*, and *Nkg7*), a lower IFN-γ production score, and down-regulation of pathways related to $CD8^+$ T cell proliferation and activation (Figure 4, G-I). These findings emphasize the potential roles of $CD138^+$ TAMs in accelerating PDAC progression by promoting tumor immune evasion. We further validated the pro-tumorigenic roles of $CD138^+$ TAMs using an orthotopic mouse model developed with Sdc1-cKO mice, in which $CD138^+$ TAMs were specifically depleted (Supplemental Figure 10E). Tumor weight was significantly reduced in Sdc1-cKO mice with orthotopic KPC tumors compared to control mice (Figure 4J and Supplemental Figure 10F). Furthermore, histopathological analysis revealed that the depletion of $CD138^+$ TAMs led to decreased cell proliferation and increased apoptosis in the tumor tissues (Figure 4, K and L and Supplemental Figure 10G). Importantly, Sdc1-cKO mice bearing orthotopic KPC tumors exhibited a dramatic increase in overall survival times compared to those in the control group (Figure 4M). To evaluate the immune status of the TME, we assessed tumor-infiltrating lymphocytes through flow cytometry and scRNA-seq. The results demonstrated a significant increase in the infiltration of $CD8^+$ T cells (Figure 4N), as well as in the fractions of T_{EM}, Tpex, intermediate Tex, Tex, and proliferating subsets among $CD8^+$ T cells within the tumor tissues of mice in the Sdc1-cKO group (Figure 4O and Supplemental Figure 10H). Furthermore, tumor-infiltrating $CD8^+$ T cells in the Sdc1-cKO group displayed signs of activation, as supported by increased expression of effector factors, a higher IFNγ production score, and up-regulation of pathways associated with T cell proliferation and activation (Figure 4, P-R). These results suggest that the depletion of $CD138^+$ TAMs can effectively hinder the development of PDAC by activating the anti-tumor immunity of $CD8^+$ cytotoxic T cells. Additionally, we investigated the tumor-promoting roles of $CD138^+$ TAMs using a chimera mouse model established by spontaneous KPC

and Sdc1-cKO mice (Supplemental Figure 10I). The results revealed a notable reduction in tumor incidence rates among the KPC/Sdc1-cKO chimera mice (Supplemental Figure 10J). Collectively, these findings underscore the substantial role of $CD138^+$ TAMs in driving the advancement of PDAC by promoting tumor immune evasion.

A feedforward loop involving $CD138^+$ TAMs and Siglec-F^+ neutrophils drives immune escape in PDAC

To explore the mechanisms by which $CD138^+$ TAMs promote immune evasion in PDAC, we first established a co-culture system using ovalbumin (OVA)-stimulated OT1 $CD8^+$ T cells and TAMs isolated from mice bearing orthotopic KPC tumors. Flow cytometric analysis revealed no significant changes in IFNγ levels in OT1 $CD8^+$ T cells when co-cultured with $CD138^+$ TAMs (Supplemental Figure 11), suggesting that $CD138^+$ TAMs do not directly influence $CD8^+$ T cell function. Given the marked crosstalk between *Sdc1*$^+$ TAMs and neutrophils revealed by CellChat (Figure 5A), the enrichment of signaling pathways related to neutrophil chemotaxis in the transcriptome of *Sdc1*$^+$ TAMs (Figure 2, C and D), and the known crucial roles of neutrophils in tumor growth and immune evasion in PDAC(43), we addressed the possibility that $CD138^+$ TAMs drive the progression of PDAC by modulating the properties of neutrophils. Sub-clustering of neutrophils based on scRNA-seq data (Supplemental Figure 5A) uncovered four distinct neutrophil subsets within the TME of orthotopic KPC mice (Figure 5B). MN1 was characterized by the expression of genes encoding cell surface proteins that bind to sialic acid (*Siglecf*) and enzymes essential for the synthesis of lipid mediators of inflammation (*Ltc4s*, *Ptgs1*, and *Cysltr1*), aligning with previously described populations(44); MN3 exhibited a unique set of interferon-stimulated genes (ISGs), including *Ifit3*, *Ifit1*, and *Irf7*, corresponding to interferon-stimulated neutrophils(45).

Other neutrophil clusters displayed high expression of ribosome-related genes (*Rps26*, *Rps12*, and *Rpl23* in MN4) and genes related to cell structure and motility (*Tmsb4x* in MN4)(46) or heat shock protein-associated genes (*Hspa1b*, *Hspa1a*, and *Hsp90aa1* in MN2) (Figure 5C). Subsequently, our data were integrated with the dataset from the pancreas of healthy mice and those with acute pancreatitis(32) to compare the fractions of neutrophil subsets (Supplemental Figure 3, A and B and Supplemental Figure 12A). The results revealed a marked increase in the proportions of MN1 and MN2 within orthotopic KPC tumors (Supplemental Figure 12B). Notably, the gene signature score of MN1, but not MN2, exhibited a significant correlation with the poor prognosis of PDAC patients, as indicated by the dataset from TCGA (Supplemental Figure 12C). Flow cytometry analysis confirmed a higher frequency of Siglec-F^+ neutrophils in the tumor tissues of orthotopic KPC mice compared to wild-type mice (Supplemental Figure 12, D-F). Thus, we conducted transcriptomic analysis of Siglec-F^+ neutrophils isolated from the orthotopic tumors using bulk RNA-seq, followed by GSEA of the scRNA-seq subsets of neutrophils based on the gene signature of these cells. The results demonstrated significant comparability in transcriptional programs between sorted Siglec-F^+ neutrophils and the MN1 subset (Figure 5D and Supplemental Figure 12G), indicating that Siglec-F can be utilized to identify the MN1 subset. Siglec-F^+Ly6g^+ cells derived from orthotopic tumors were confirmed to be a subset of neutrophils, as evidenced by their multi-lobed nuclei and pale pink cytoplasm containing fine, light purple granules, which were visible through Wright-Giemsa staining. Additionally, these cells exhibited minimal expression of CCR3 (Supplemental Figure 12H). Notably, a significant increase in the proportion of Siglec-F^+ neutrophils was observed in the tumor tissues of orthotopic KPC mice following the adoptive transfer of $CD138^+$ TAMs (Figure 5, E-G). However, the depletion of $CD138^+$ TAMs through genetic ablation of IL-34-syndecan-1 signaling using Sdc1-cKO mice resulted in a significant

decrease in the proportion of the neutrophil subset within orthotopic tumors (Figure 5, H-J). Furthermore, a notable increase in the frequency of SIGLEC-8$^+$ neutrophils, which correspond to the human equivalent of murine Siglec-F$^+$ neutrophils(47), was observed in the primary tumors of PDAC patients from Cohort 2 (Figure 5, K and L). To investigate the correlation among CD138$^+$ TAMs, SIGLEC-8$^+$ neutrophils, and tumor cells in patients, we conducted a mIHC assay on tissue arrays derived from Cohort 2 and 3. Our findings indicated a positive correlation between the frequency of SIGLEC-8$^+$ neutrophils and CD138$^+$ TAMs, as well as between the abundance of SIGLEC-8$^+$ neutrophils and tumor cells in the tumor tissues of these patients (Figure 5, M-O, and Supplemental Figure 1B). Furthermore, the analysis of localization patterns revealed that CD138$^+$ TAMs exhibited significantly higher effective scores and percentages, two indicators that integrate both cell proximity and numbers to evaluate cell distribution(48), compared to CD138$^-$ TAMs (Supplemental Figure 12, I-L). This suggests a co-localization and effective cell-to-cell interaction between CD138$^+$ TAMs and SIGLEC-8$^+$ neutrophils. Notably, the presence of SIGLEC-8$^+$ neutrophils was correlated with negative outcomes in patients with PDAC (Figure 5P). Patients with elevated levels of both CD138$^+$ TAMs and SIGLEC-8$^+$ neutrophils exhibited the most unfavorable prognosis (Figure 5Q). Altogether, these findings imply a potential influence of CD138$^+$ TAMs on the activity and accumulation of Siglec-F$^+$ (SIGLEC-8$^+$) neutrophils and the pro-tumorigenic roles of this neutrophil subset.

To investigate whether CD138$^+$ TAMs directly influence the characteristics of Siglec-F$^+$ neutrophils, neutrophils extracted from the bone marrow of wild-type mice were exposed to conditioned medium (CM) derived from either CD138$^+$ or CD138$^-$ TAMs (Figure 6A). The results revealed a significant increase in the proportions of Siglec-F$^+$ neutrophils when exposed to CD138$^+$ TAM-CM (Figure 6, B and C). A similar phenomenon was observed in cultures of human

peripheral blood-derived neutrophils (PBDNs) when exposed to $CD138^+$ TAM-CM from PDAC patients (Figure 6, D and E). In vitro chemotaxis analysis (Figure 6F) demonstrated that $CD138^+$ TAM-CM markedly enhanced neutrophil trafficking, in comparison to $CD138^-$ TAM-CM (Figure 6G). Phenotypic analysis indicated that $CD138^+$ TAMs exhibited elevated expression levels of factors that mediate neutrophil properties, such as SAA3 and CXCL1(49) (Figure 2, B-G and Supplemental Figure 3F). Further examination of the impacts of SAA3 and CXCL1 expressed by $CD138^+$ TAMs on neutrophil characteristics, using bone marrow-derived neutrophil (BMDN) culture systems (Figure 6, A and F), revealed that SAA3 promoted the polarization of Siglec-F^+ neutrophils (Figure 6, H and I), while CXCL1 enhanced neutrophil migration (Figure 6J). This observation was corroborated by the blockade of BMDN polarization into Siglec-F^+ neutrophils induced by $CD138^+$ TAM-CM using anti-SAA3 neutralizing antibodies (Figure 6, K and L). To explore the mechanism by which SAA3 induces the polarization of Siglec-F^+ neutrophils, we conducted KEGG enrichment analysis of differentially expressed genes (DEGs) in Siglec-F^+ neutrophils utilizing bulk RNA-seq data. The results indicated that the up-regulated genes in these cells were significantly enriched in MAPK signaling pathways (Figure 6M), a canonical downstream pathway of SAA3(50–52). Upon introducing inhibitors targeting the p38 MAPK pathway and FPR2 (a primary receptor of SAA3(52)) into the BMDN cultures, we found that both inhibitors markedly impeded the polarization of BMDNs into Siglec-F^+ neutrophils (Figure 6, N and O). These phenomena suggest that SAA3 induces the polarization of Siglec-F^+ neutrophils through binding to FPR2 and subsequently stimulating the p38 MAPK pathway. Collectively, these findings demonstrate that $CD138^+$ TAMs play a crucial role in regulating the polarization and migration of Siglec-F^+ neutrophils through the actions of SAA3 and CXCL1.

We next explore whether and how Siglec-F$^+$ neutrophils promote immune evasion in PDAC. Analysis of bulk RNA-seq data revealed that genes up-regulated in Siglec-F$^+$ neutrophils were significantly enriched in pathways related to arachidonic acid metabolism and NET formation, as defined by KEGG terms (Figure 6M). Furthermore, Siglec-F$^+$ neutrophils exhibited a greater capacity for NET formation in in-vitro cultures compared to their Siglec-F$^-$ counterparts (Figure 7, A and B). NET formation has been implicated in the exclusion and dysfunction of CD8$^+$ T cells within the TME(53, 54). Notably, our results demonstrated the activation of CD8$^+$ T cells in orthotopic tumors following the depletion of CD138$^+$ TAMs via the genetic ablation of IL-34-syndecan-1 signaling (Figure 4, N-R and Supplemental Figure 10H). Thus, we examined whether Siglec-F$^+$ neutrophils exert direct effects on CD8$^+$ T cells. To this end, we established a co-culture system utilizing OVA-activated OT1 CD8$^+$ T cells and neutrophils isolated from orthotopic tumors. Flow cytometry analysis showed a significant reduction in IFNγ levels in OT1 CD8$^+$ T cells when co-cultured with Siglec-F$^+$ neutrophils, as opposed to those co-cultured with Siglec-F$^-$ neutrophils (Figure 7, C and D). Importantly, SIGLEC-8$^+$ neutrophils isolated from the tumor tissues of PDAC patients exhibited similar inhibitory effects on CD8$^+$ T cells (Figure 7, E and F). This suggests that Siglec-F$^+$ neutrophils possess the ability to impair the cytotoxicity of CD8$^+$ T cells. To investigate whether CD138$^+$ TAMs hinder the cytotoxicity of CD8$^+$ T cells by modulating the properties of neutrophils, BMDNs exposed to CM from either CD138$^+$ or CD138$^-$ TAMs were introduced into the co-culture system (Figure 7G). It was observed that only neutrophils primed by CD138$^+$ TAM-CM were capable of reducing IFNγ levels in OT1 CD8$^+$ T cells (Figure 7, H and I). Notably, neutrophils treated with SAA3 (Figure 7G), a factor that is highly expressed by CD138$^+$ TAMs, exhibited similar immunosuppressive effects on CD8$^+$ T cells (Figure 7, J and K). These findings indicate that CD138$^+$ TAMs impair the anti-tumor functions of CD8$^+$ T cells by stimulating the

polarization of Siglec-F^+ neutrophils via the influence of SAA3. It is widely recognized that PGE_2 is a major metabolite of arachidonic acid metabolism(55), leading to the hypothesis that these cells inversely up-regulate the expression of syndecan-1 on TAMs by secreting PGE_2, thereby promoting the generation of $CD138^+$ TAMs. An enzyme-linked immunosorbent assay (ELISA) confirmed a marked elevation in PGE_2 levels in the CM from Siglec-F^+ neutrophils (Figure 7L). Subsequently, BMDMs isolated from wild-type mice were exposed to CM from either Siglec-F^+ or Siglec-F^- neutrophils derived from orthotopic tumors (Figure 7M). Flow cytometry analysis revealed a marked increase in CD138 expression on BMDMs in the group treated with Siglec-F^+ neutrophil-CM compared to those exposed to Siglec-F^- neutrophil-CM (Figure 7, N and O). Furthermore, we observed a synergistic effect between $CD138^+$ TAMs and Siglec-F^+ neutrophils on the functional impairment of $CD8^+$ T cells in co-culture systems, although $CD138^+$ TAMs alone did not affect their functions (Supplemental Figure 13). Taken together, these findings demonstrate the presence of a feedforward loop between $CD138^+$ TAMs and Siglec-F^+ neutrophils in the TME, which results in immune evasion in PDAC by suppressing the anti-tumor activities of $CD8^+$ T cells. We then investigated the presence of this loop in other cancer types. The results indicated a significant increase in the abundance of $CD138^+$ TAMs and SIGLEC-8^+ neutrophils in the tumor tissues of patients with hepatocellular carcinoma (HCC). In contrast, such an increase was not observed in patients with intrahepatic cholangiocarcinoma (ICC) (Supplemental Figure 14). Given that both IL-34 and PGE_2 levels were elevated and correlated with tumor progression and metastasis in HCC, but not in ICC(56, 57), we speculate that the $CD138^+$ TAM-Siglec-F^+ neutrophil axis may have developed in cancer types characterized by elevated levels of both IL-34 and PGE_2.

Anti-IL-34 antibodies in combination with anti-PD-1 immunotherapy effectively abrogate the progression of PDAC

Next, we investigated the impact of disrupting the feedforward loop between $CD138^+$ TAMs and Siglec-F^+ neutrophils by blocking IL-34-syndecan-1 signaling on the PDAC progression. Given that flow cytometric results indicated that these two subsets prominently emerged 14 days after tumor implantation (Supplemental Figure 15), anti-IL-34 antibodies were administered intraperitoneally to orthotopic KPC mice bi-daily, commencing nine days post-tumor injection, with tumor tissues harvested 21 days after implantation (Figure 8A). A marked reduction in tumor weight was observed in the anti-IL-34 antibody treatment group (Figure 8B and Supplemental Figure 16A). Pathological analysis revealed that treatment with anti-IL-34 antibodies led to decreased cell proliferation and increased apoptosis within the tumor tissues (Figure 8, C and D and Supplemental Figure 16B). Notably, survival analysis demonstrated a significant increase in overall survival times for mice receiving anti-IL-34 antibody treatment compared to the control group (Figure 8E).

To determine whether the therapeutic effects of anti-IL-34 antibodies depend on the blockade of the $CD138^+$ TAM-Siglec-F^+ neutrophil axis, we examined the cellular compositions within the TME of orthotopic KPC mice following treatment with anti-IL-34 antibodies. The results demonstrated a significant reduction in the percentage of $CD138^+$ TAMs and Siglec-F^+ neutrophils (Figure 8, F-N), accompanied by a notable increase in the frequencies of $CD8^+$ T cells post-treatment with anti-IL-34 antibodies, although other effector cell subsets did not exhibit significant alterations (Figure 8O). Subsequent phenotypic analysis revealed an expansion of effector $CD8^+$ T cells; nevertheless a considerable proportion of $CD8^+$ T cells displayed a late-exhausted state, and NK cells were not activated within the TME (Figure 8, P-S and Supplemental Figure 16, C-

G). This indicates that T cell exhaustion occurs in the PDAC TME during treatment with anti-IL-34 antibodies. Thus, a therapeutic strategy combining anti-IL-34 antibodies with anti-PD-1 immunotherapy was evaluated in orthotopic KPC mice (Figure 8A). The results revealed a notable delay in tumor progression in mice receiving the combination therapy compared to those treated with single agents (Figure 8, B-D and Supplemental Figure 16, A and B). More importantly, mice treated with the combination therapy exhibited remarkably longer survival times than those in the control groups (Figure 8E). Subsequently, we assessed the immune status of the TME in mice that underwent combination therapy. The results revealed a marked increase in the percentages of $CD8^+$ T cells and effector $CD8^+$ T cells, alongside a substantial reduction in late-exhausted $CD8^+$ T cells (Figure 8, O-S and Supplemental Figure 16, C-E). Furthermore, NK cells within the TME did not exhibit significant activation (Supplemental Figure 16, F and G). These observations demonstrate that anti-PD-1 immunotherapy enhances therapeutic efficacy against PDAC by reversing $CD8^+$ T cell exhaustion within the TME when combined with anti-IL-34 antibodies. Notably, the combination therapy continued to prolong overall survival times in orthotopic KPC mice, even when initiated 21 days post-tumor implantation (Figure 8T). Considering that $CD138^+$ TAMs drive the polarization of Siglec-F^+ neutrophils through the activation of the SAA3/FPR2/p38 MAPK pathway, we tested a therapeutic strategy that combined anti-IL-34 antibodies, anti-PD-1 antibodies, and WRW4 (a FPR2 antagonist) in orthotopic KPC mice. Unexpectedly, survival analysis revealed no improvement in overall survival times in mice when WRW4 was introduced into the therapeutic strategy (Supplemental Figure 16H). Collectively, these findings indicate that anti-IL-34 antibodies dramatically enhance the management of PDAC by impeding the immunosuppressive feedforward loop between $CD138^+$ TAMs and Siglec-F^+ neutrophils, and

demonstrate improved therapeutic effects, particularly when combined with anti-PD-1 immunotherapy.

Discussion

Over the past few decades, numerous studies have explored the potential of immunotherapy to improve overall survival in patients with PDAC and in mouse models(58). However, the majority of immunotherapy strategies, whether administered alone or in combination, have proven ineffective, primarily due to the tumor's ability to evade the immune system. This study identifies the emergence of a unique population of $CD138^+$ TAMs that expands in both PDAC patients and mouse models, characterized by pro-inflammatory and neutrophil-chemotactic activity. This expansion correlates with tumor immune escape and unfavorable outcomes in patients, and is crucial for immune evasion and disease progression in mice. Through phenotypic and functional analyses, we determined that these cells establish a reciprocal relationship with immunosuppressive Siglec-F^+ neutrophils by secreting SAA3 and CXCL1. This interaction facilitates PDAC immune evasion by hindering the cytotoxic actions of $CD8^+$ T cells. By blocking the generation of $CD138^+$ TAMs, the progression of pancreatic tumors can be prevented, particularly when combined with anti-PD-1 immunotherapy. Thus, our findings propose a combinatorial therapeutic strategy to impede the advancement of PDAC.

It should be noted that although both IL-34 and PGE_2 have been reported to promote M2 polarization of macrophages in acute inflammation and several cancer types(17, 18, 24, 59, 60), their combined actions have been rarely mentioned. To the best of our knowledge, this study provides the initial documentation of a localized synergy between IL-34-syndecan-1 and PGE_2-EP2 signaling in the polarization of tumor-infiltrating monocytes into pro-inflammatory $CD138^+$

TAMs. The underlying mechanism involves the activation of the PI3K/Akt/NFκB signaling pathway by IL-34, in conjunction with the EPAC/Rap1 pathway stimulated by PGE_2. Supporting this model, previous studies have demonstrated the following: (1) Up-regulation of both IL-34 and COX-2 in PDAC has been observed (35–37, 61). (2) PGE_2 exerts regulatory effects on syndecan-1 expression in macrophages(24, 62). (3) Syndecan-1 acts as a functional receptor for IL-34 in macrophages(19, 34, 59). (4) Macrophages induced by IL-34 promote the polarization of Th1/Th17 cells in rheumatoid arthritis, a chronic inflammatory environment (32). (5) PGE_2 facilitates tumor immune escape through the impairment of antigen presentation by Cxcl9/10^+ inflammatory monocytes(63). Thus, in response to the chronic, dysregulated, persistent, and unresolved inflammatory state within the PDAC TME(64), tumor-infiltrating monocytes likely undergo a distinct differentiation program, giving rise to an atypical pro-inflammatory macrophage subtype in PDAC.

Both TAMs and tumor-infiltrating neutrophils play crucial roles in tumor immune escape(65). Several studies have documented a bidirectional interplay between these two myeloid cell types within tumors(66, 67). However, the specific interactions between TAMs and neutrophils in the TME of PDAC have not been extensively explored. This study emphasizes a role of SAA3, secreted by $CD138^+$ TAMs, in polarizing tumor-infiltrating neutrophils towards an immunosuppressive Siglec-F^+ phenotype, characterized by enhanced synthesis of PGE_2 and the release of NETs. This process occurs through the binding of SAA3 to FPR2, subsequently activating the p38 MAPK signaling pathway in neutrophils. In turn, Siglec-F^+ neutrophils facilitate syndecan-1 expression via PGE_2 production, which further enhances IL-34-syndecan-1 signaling in TAMs. This interaction creates a feedforward loop that ultimately drives immune evasion in PDAC. Notably, the emergence of a small number of $CD138^+$ macrophages in adjacent benign

tissues of PDAC patients and in the pancreatic tissues of wild-type mice suggests that this feedforward loop is initially driven by gradually increasing levels of IL-34 secreted by tumor cells during the early stages of pancreatic cancer. Furthermore, the elevated expression levels of *Ptgs2* in tumor-infiltrating neutrophils prior to the establishment of this loop suggest that these cells provide the initiating PGE_2 signal necessary to trigger this loop.

Our preclinical studies demonstrate that the administration of anti-IL-34 antibodies effectively inhibits the progression of pancreatic tumors by enhancing the anti-tumor responses of effector $CD8^+$ T cells. Notably, these antibodies exhibit improved therapeutic effects when combined with anti-PD-1 immunotherapy. In contrast, anti-PD-1 antibodies administered independently do not enhance overall survival in mice. Similar trends have been reported in clinical trials, where PDAC tumors show limited responsiveness to anti-PD-1 immunotherapies(58, 68). Thus, these findings indicate that targeting $CD138^+$ TAMs through the blockade of IL-34-syndecan-1 signaling facilitates a transition of the PDAC TME from immunosuppressive to immunoreactive. This transition may enable anti-IL-34 antibodies to effectively synergize with anti-PD-1 immunotherapy, potentially converting entirely unresponsive PDAC tumors into responsive ones in clinical settings. Our findings indicate that the introduction of the FPR2 antagonist into the combination therapeutic strategy did not confer any benefit in overall survival times in mice. This lack of improvement may be attributed to the presence of multiple ligands of FPR2, including lipoxin A4, which has been reported to play inhibitory roles in tumor progression and metastasis of PDAC(69, 70).

In summary, we have identified a unique population of $CD138^+$ TAMs elicited by IL-34 and PGE_2 in both PDAC patients and mouse models. This specific TAM subset establishes a feedforward loop with immunosuppressive PGE_2-secreting Siglec-F^+ neutrophils through the

actions of SAA3 and CXCL1, which leads to immune evasion and thereby fosters a pro-tumor TME. Targeting this population with anti-IL-34 antibodies may yield clinical benefits for PDAC patients, especially when combined with anti-PD-1 immunotherapy. Therefore, the combined application of anti-IL-34 and anti-PD-1 antibodies may sustain anti-tumor responses, providing a therapeutic avenue for improved PDAC management.

Methods

Sex as a biological variable

This study included both male and female patients, as well as healthy donors, ensuring that there was no bias in the grouping. The results were consistent regardless of gender. All animal experiments were conducted using male mice.

Patient samples

Fresh tissue and serum samples were collected from patients with PDAC in Cohort 1, all of whom underwent surgical resection at the First Affiliated Hospital, Zhejiang University School of Medicine. This cohort comprised 103 PDAC patients who had not received any prior treatments. Additionally, a total of 41 paired adjacent benign and tumor tissues from PDAC patients in Cohort 2, along with 156 unpaired tumor tissues from patients in Cohort 3 were utilized to create two distinct tissue arrays at Wuhan Servicebio Technology. Detailed patient information for Cohort 3, which includes data on 114 patients with available prognostic information, is provided in Supplemental Data file 1. Patients in Cohort 3 were stratified into groups according to the abundance of $CD138^+$ TAMs and/or the frequency of SIGLEC-8^+ neutrophils, utilizing the optimal p-value cutoff determined by the Mann-Whitney test. A total of 13 patients with HCC and 15

patients with ICC underwent surgical resection at the First Affiliated Hospital of Zhejiang University School of Medicine, from which paired adjacent benign and tumor tissues were collected for the preparation of tissue sections.

Animals

Male *C57BL/6* mice aged 6 to 8 weeks were purchased from the Model Animal Research Center of Nanjing University in China. The *Kras*$^{LSL\text{-}G12D}$, *Trp53*$^{LSL\text{-}R172H}$, and *Pdx-1-cre* genetically engineered mice were procured from the Jackson Laboratory and subsequently crossed to generate the spontaneous KPC mouse model. *Kras*$^{LSL\text{-}G12D}$*; TgfβR2*$^{flox/flox}$*; Ptf1a-cre* (KTC) mice were generously provided by Prof. Hideaki Ijichi (Department of Gastroenterology at the University of Tokyo, Bunkyo-ku, Tokyo, Japan) and Harold L Moses (Department of Cancer Biology at Vanderbilt-Ingram Cancer Center, Nashville, Tennessee, USA). *Ptger2-flox* (Strain NO. T018685), *Sdc1-flox* (Strain NO. T015943), and *Csf1r-Cre* (Strain NO. T005640) mice were acquired from GemPharmatech (Nanjing, China). *Ptger2-flox* and *Sdc1-flox* mice were crossed with *Csf1r-Cre* mice to generate *Ptger2*$^{flox/flox}$*; Csf1r-Cre* (Ptger2-cKO) and *Sdc1*$^{flox/flox}$*; Csf1r-Cre* (Sdc1-cKO) mice, respectively. All mice were maintained under specific-pathogen-free conditions at the Experimental Animal Center of the First Affiliated Hospital, Zhejiang University School of Medicine.

For the orthotopic tumor models, a total of $5X10^5$ KPC cells were resuspended in cold PBS and mixed at a 1:1 dilution with Matrigel (Corning) to achieve a final volume of 25μl, which was then injected into the pancreas. Mice were euthanized on day 21 post-tumor implantation, except for those designated for survival analysis. The endpoint of the survival analysis was defined as the time at which all mice in either the control or experimental group had succumbed.

Anti-IL-34 and/or anti-PD-1 antibody and/or WRW4 treatment in vivo

Mice were intraperitoneally injected with 200μg of anti-IL-34 antibody (Cat MAB5195, R&D Systems) every other day, totaling six doses, starting on Day 9 after the orthotopic inoculation of $5X10^5$ KPC cells. Anti-PD-1 antibody (200μg/mice, Cat BE0146, Bioxcell) was administered intraperitoneally on 12 and 16 days post-tumor implantation. WRW4 (1mg/kg, MedChemExpress) was injected intraperitoneally daily, commencing on Day 9 following tumor implantation. At 21 days post-injection, all mice were sacrificed, except for those designated for survival analysis. The endpoint of the survival analysis was determined as the time at which all mice in the control group had perished. Tumor tissues were collected for flow cytometric analysis or immunohistochemical staining. For the survival analysis of the combination therapy against advanced tumors, the administration of anti-IL-34 antibodies began on Day 21, while anti-PD-1 antibodies were injected starting on Day 24 following tumor implantation.

Statistics

Statistical analyses were conducted using GraphPad Prism 9. Results are presented as mean ± standard error of the mean (SEM), with significance evaluated through unpaired or paired two-tailed Student's t-tests, unless otherwise specified. P-values less than 0.05 were considered statistically significant. For correlation assessments, either Pearson's or Spearman's correlation analyses were utilized. Differences in survival analysis were determined using the log-rank test. The optimal cutoff point for patients in Cohort 3 was calculated using Mann-Whitney tests within SPSS Statistics software. Bioinformatics statistical analyses were performed in R (v4.4.1). For comparisons between two groups, the Wilcoxon rank-sum test was employed to assess differences

in population means, with significance defined as a p-value less than 0.05, unless otherwise indicated.

Study approval

All participants provided signed informed consent and the research protocol was approved by the Ethics Committee of the First Affiliated Hospital, Zhejiang University School of Medicine (IIT20210023B-R1). The animal experiments were conducted in strict accordance with the guidelines and standards approved by the Institutional Animal Care and Use Committee (IACUC).

Data availability

The datasets generated and/or analyzed during the current study are available in the Genome Sequence Archive (GSA) under accession number CRA017890. The data reanalyzed for this study can be accessed in the Gene Expression Omnibus (GEO) using the accession code GSE217846, which pertains to the scRNA-seq of blood samples from orthotopic KPC mice. Additionally, the scRNA-seq data of healthy pancreas and acute pancreatitis in mice can be found in the European Nucleotide Archive (ENA) browser under the project identifier PRJNA978570. All code utilized in this study is accessible at https://jhuanglab.github.io/sdc1_mac/. Values for all data points in graphs are reported in the Supporting Data Values file.

Author contributions

CW, QZ, TL, and TL designed the experiments and interpreted the data; CW, FL, YM, and JT performed most of the experiments; FL performed clinical relevance analysis; JH, DZ, YL, TZ, and JL performed the bioinformatics analysis; FS and HS assisted in some experiments; CW and TL wrote the manuscript and provided overall guidance. CW, QZ, and JH are co-first authors; the order of authorship reflects the extent to which each author contributed to the key developments in this work.

Funding support

This work was financially supported by National Key Research and Development Program of China (2020YFA0804300 to QZ), National Natural Science Foundation of China (82188102 and U20A20378 to TL, 82003016 to CW, 92474310, 32321002 and 82273338 to QZ), Natural Science Foundation of Zhejiang Province (LQ21H160017 to CW), and Fundamental and Interdisciplinary Disciplines Breakthrough Plan of the Ministry of Education of China (JYB2025XDXM611 to TL).

Acknowledgments

We thank Prof. Xiongbin Lu, Haojie Huang from Zhejiang University and Jun Qin from Shanghai Institute of Nutrition and Health, CAS for their valuable suggestions and editing.

References

1. Siegel RL, Giaquinto AN, Jemal A. Cancer statistics, 2024. *CA Cancer J Clin*. 2024;74(1):12–49.

2. Ho WJ, Jaffee EM, Zheng L. The tumour microenvironment in pancreatic cancer — clinical challenges and opportunities. *Nat Rev Clin Oncol*. 2020;17(9):527–540.

3. Habtezion A, Edderkaoui M, Pandol SJ. Macrophages and pancreatic ductal adenocarcinoma. *Cancer Lett*. 2016;381(1):211–216.

4. Liu X, et al. Context-dependent activation of STING-interferon signaling by CD11b agonists enhances anti-tumor immunity. *Cancer Cell*. 2023;41(6):1073-1090.e12.

5. Biswas SK, Mantovani A. Macrophage plasticity and interaction with lymphocyte subsets: Cancer as a paradigm. *Nat Immunol*. 2010;11(10):889–896.

6. Caronni N, et al. IL-1β+ macrophages fuel pathogenic inflammation in pancreatic cancer. *Nature*. 2023;623(7986):415–422.

7. Sun X, et al. Inflammatory cell-derived CXCL3 promotes pancreatic cancer metastasis through a novel myofibroblast-hijacked cancer escape mechanism. *Gut*. 2022;71(1):129–147.

8. Nielsen SR, et al. Macrophage-secreted granulin supports pancreatic cancer metastasis by inducing liver fibrosis. *Nat Cell Biol*. 2016;18(5):549–560.

9. Wang Y, et al. Anti-PD-1/L1 lead-in before MAPK inhibitor combination maximizes antitumor immunity and efficacy. *Cancer Cell*. 2021;39(10):1375-1387.e6.

10. Hezaveh K, et al. Tryptophan-derived microbial metabolites activate the aryl hydrocarbon receptor in tumor-associated macrophages to suppress anti-tumor immunity. *Immunity*. 2022;55(2):324-340.e8.

11. Bian Z, et al. Intratumoral SIRPα-deficient macrophages activate tumor antigen-specific cytotoxic T cells under radiotherapy. *Nat Commun*. 2021;12(1):1–16.

12. Pan Z, et al. VSIG4+ tumor-associated macrophages mediate neutrophil infiltration and impair antigen-specific immunity in aggressive cancers through epigenetic regulation of SPP1. *J Exp Clin Cancer Res*. 2025;44(1):45.

13. Hu J, et al. Tumor microenvironment remodeling after neoadjuvant immunotherapy in non-small cell lung cancer revealed by single-cell RNA sequencing. *Genome Med*. 2023;15(1):14.

14. Luckett T, et al. Mesothelin Secretion by Pancreatic Cancer Cells Co-opts Macrophages and Promotes Metastasis. *Cancer Res*. 2024;84(4):527–544.

15. Nywening TM, et al. Targeting both tumour-associated CXCR2+ neutrophils and CCR2+ macrophages disrupts myeloid recruitment and improves chemotherapeutic responses in pancreatic ductal adenocarcinoma. *Gut*. 2018;67(6):1112–1123.

16. Baghdadi M, et al. Interleukin-34, a comprehensive review. *J Leukoc Biol*. 2018;104(5):931–951.

17. Franzè E, et al. Role of Interleukin-34 in Cancer. *Cancers (Basel)*. 2020;12(1):252.

18. Nian Z, et al. Interleukin-34-orchestrated tumor-associated macrophage reprogramming is required for tumor immune escape driven by p53 inactivation. *Immunity*. 2024;57(10):2344-2361.e7.

19. Segaliny AI, et al. Syndecan-1 regulates the biological activities of interleukin-34. *Biochim Biophys Acta - Mol Cell Res*. 2015;1853(5):1010–1021.

20. Yao W, et al. Syndecan 1 is a critical mediator of macropinocytosis in pancreatic cancer. *Nature*. 2019;568(7752):410–414.

21. Hingorani SR, et al. Trp53R172H and KrasG12D cooperate to promote chromosomal instability and widely metastatic pancreatic ductal adenocarcinoma in mice. *Cancer Cell*. 2005;7(5):469–483.

22. Ijichi H, et al. Aggressive pancreatic ductal adenocarcinoma in mice caused by pancreas-specific blockade of transforming growth factor-β signaling in cooperation with active Kras expression. *Genes Dev*. 2006;20(22):3147–3160.

23. Han S, et al. A Novel Subset of Anti-Inflammatory CD138 + Macrophages Is Deficient in Mice with Experimental Lupus . *J Immunol*. 2017;199(4):1261–1274.

24. Kim C, et al. Antiinflammatory cAMP signaling and cell migration genes co-opted by the anthrax bacillus. *Proc Natl Acad Sci U S A*. 2008;105(16):6150–6155.

25. Xiao J, et al. Syndecan-1 displays a protective role in aortic aneurysm formation by modulating T cell-mediated responses. *Arterioscler Thromb Vasc Biol*. 2012;32(2):386–396.

26. Conti M, Beavo J. Biochemistry and physiology of cyclic nucleotide phosphodiesterases: Essential components in cyclic nucleotide signaling. *Annu Rev Biochem*. 2007;76:481–511.

27. Yu Y, et al. Unraveling the role of M1 macrophage and CXCL9 in predicting immune checkpoint inhibitor efficacy through multicohort analysis and single-cell RNA sequencing. *MedComm*. 2024;5(3):1–18.

737 28. Chen X, et al. Identification of FCN1 as a novel macrophage infiltration-associated biomarker
738 for diagnosis of pediatric inflammatory bowel diseases. *J Transl Med*. 2023;21(1):1–17.

739 29. Ho WS, et al. PP2Ac/STRN4 negatively regulates STING-type i IFN signaling in tumor-
740 associated macrophages. *J Clin Invest*. 2023;133(6):e162139.

741 30. König J, et al. Myeloid Mir34a suppresses colitis-associated colon cancer: characterization of
742 mediators by single-cell RNA sequencing. *Cell Death Differ.* 2025;32(2):225-241.

743 31. Zhang K, et al. TREM2hi resident macrophages protect the septic heart by maintaining
744 cardiomyocyte homeostasis. *Nat Metab*. 2023;5(1):129–146.

745 32. Aney KJ, et al. Novel Approach for Pancreas Transcriptomics Reveals the Cellular Landscape
746 in Homeostasis and Acute Pancreatitis. *Gastroenterology*. 2024;166(6):1100–1113.

747 33. Djurec M, et al. Saa3 is a key mediator of the protumorigenic properties of cancer-associated
748 fibroblasts in pancreatic tumors. *Proc Natl Acad Sci U S A*. 2018;115(6):E1147–E1156.

749 34. Van Raemdonck K, et al. Interleukin-34 Reprograms Glycolytic and Osteoclastic Rheumatoid
750 Arthritis Macrophages via Syndecan 1 and Macrophage Colony-Stimulating Factor Receptor.
751 *Arthritis Rheumatol*. 2021;73(11):2003–2014.

752 35. Okami J, et al. Overexpression of cyclooxygenase-2 in carcinoma of the pancreas. *Clin Cancer*
753 *Res*. 1999;5(8):2018–2024.

754 36. Tucker ON, et al. Cyclooxygenase-2 expression is up-regulated in human pancreatic cancer.
755 *Cancer Res*. 1999;59(5):987–990.

756 37. Yoshida S, et al. Pancreatic Stellate Cells (PSCs) express cyclooxygenase-2 (COX-2) and
757 pancreatic cancer stimulates COX-2 in PSCs. *Mol Cancer*. 2005;4:1–9.

758 38. Wang D, Dubois RN. Prostaglandins and cancer. *Gut*. 2006;55(1):115–122.

759 39. Rahnama'i MS, et al. The role of prostanoids in urinary bladder physiology. *Nat Rev Urol*.
760 2012;9(5):283–290.

761 40. Rapraeger AC. Synstatin: A selective inhibitor of the syndecan-1-coupled IGF1R-αvβ3
762 integrin complex in tumorigenesis and angiogenesis. *FEBS J*. 2013;280(10):2207–2215.

763 41. Jiang J, Dingledine R. Prostaglandin receptor EP2 in the crosshairs of anti-inflammation, anti-
764 cancer, and neuroprotection. *Trends Pharmacol Sci*. 2013;34(7):413–423.

765 42. Otsuka R, Wada H, Seino K ichiro. IL-34, the rationale for its expression in physiological and
766 pathological conditions. *Semin Immunol*. 2021;54(June):101517.

767 43. Bianchi A, et al. Cell-Autonomous Cxcl1 Sustains Tolerogenic Circuitries and Stromal
768 Inflammation via Neutrophil-Derived TNF in Pancreatic Cancer. *Cancer Discov*.
769 2023;13(6):1428–1453.

770 44. Shin JW, et al. A unique population of neutrophils generated by air pollutant–induced lung
771 damage exacerbates airway inflammation. *J Allergy Clin Immunol*. 2022;149(4):1253-1269.e8.

772 45. Xie X, et al. Single-cell transcriptome profiling reveals neutrophil heterogeneity in homeostasis
773 and infection. *Nat Immunol*. 2020;21(9):1119–1133.

774 46. Keenum MC, et al. Single-cell epitope-transcriptomics reveal lung stromal and immune cell
775 response kinetics to nanoparticle-delivered RIG-I and TLR4 agonists. *Biomaterials*.
776 2023;297(December 2022):122097.

777 47. Ryu S, et al. Siglec-F–expressing neutrophils are essential for creating a profibrotic
778 microenvironment in renal fibrosis. *J Clin Invest*. 2022;132(12):e156876.

779 48. Jia K, et al. Multiplex immunohistochemistry defines the tumor immune microenvironment
780 and immunotherapeutic outcome in CLDN18.2-positive gastric cancer. *BMC Med*. 2022;20(1):1–
781 15.

782 49. De Santo C, et al. Invariant NKT cells modulate the suppressive activity of IL-10-secreting
783 neutrophils differentiated with serum amyloid A. *Nat Immunol*. 2010;11(11):1039–1046.

784 50. Deguchi A, et al. Serum Amyloid A3 Binds MD-2 To Activate p38 and NF-κB Pathways in a
785 MyD88-Dependent Manner. *J Immunol*. 2013;191(4):1856–1864.

786 51. Lin A, et al. Serum amyloid A inhibits astrocyte migration via activating p38 MAPK. *J*
787 *Neuroinflammation*. 2020;17(1):1–14.

788 52. Chen X, et al. FPR2 deficiency alleviates diet-induced insulin resistance through reducing body
789 weight gain and inhibiting inflammation mediated by macrophage chemotaxis and M1 polarization.
790 *Diabetes*. 2019;68(6):1130–1142.

791 53. Taifour T, et al. The tumor-derived cytokine Chi3l1 induces neutrophil extracellular traps that
792 promote T cell exclusion in triple-negative breast cancer. *Immunity*. 2023;56(12):2755-2772.e8.

793 54. Song M, et al. DNA of Neutrophil Extracellular Traps Binds TMCO6 to Impair CD8+ T-cell
794 Immunity in Hepatocellular Carcinoma. *Cancer Res*. 2024;84(10):1613–1629.

795 55. Goodman M, Barrell G. Prostaglandins, Arachidonic Acid, and Inflammation. *Science*.
796 1980;210(4473):978–984.

797 56. Dong XF, et al. COX-2/PGE2 axis regulates HIF2a activity to promote hepatocellular
798 carcinoma hypoxic response and reduce the sensitivity of sorafenib treatment. *Clin Cancer Res*.
799 2018;24(13):3204–3216.

800 57. Zhou SL, et al. miR-28-5p-IL-34-macrophage feedback loop modulates hepatocellular
801 carcinoma metastasis. *Hepatology*. 2016;63(5):1560–1575.

802 58. Hilmi M, et al. The immunological landscape in pancreatic ductal adenocarcinoma and
803 overcoming resistance to immunotherapy. *Lancet Gastroenterol Hepatol*. 2023;8(12):1129–1142.

804 59. Bézie S, et al. IL-34 Actions on FOXP3+ Tregs and CD14+ Monocytes Control Human Graft
805 Rejection. *Front Immunol*. 2020;11(August):1–16.

806 60. Ruze R, et al. Enhanced cytokine signaling and ferroptosis defense interplay initiates obesity-
807 associated pancreatic ductal adenocarcinoma. *Cancer Lett*. 2024;601(August):217162.

808 61. Candido JB, et al. CSF1R+ Macrophages Sustain Pancreatic Tumor Growth through T Cell
809 Suppression and Maintenance of Key Gene Programs that Define the Squamous Subtype. *Cell Rep*.
810 2018;23(5):1448–1460.

811 62. Yeaman C, Rapraeger AC. Post-transcriptional regulation of syndecan-1 expression by cAMP
812 in peritoneal macrophages. *J Cell Biol*. 1993;122(4):941–950.

813 63. Elewaut A, et al. *Cancer cells impair monocyte-mediated T cell stimulation to evade*
814 *immunity.Nature*. 2025;637(8046):716-725.

815 64. Elinav E, et al. Inflammation-induced cancer: Crosstalk between tumours, immune cells and
816 microorganisms. *Nat Rev Cancer*. 2013;13(11):759–771.

817 65. Hingorani SR. Epithelial and stromal co-evolution and complicity in pancreatic cancer. *Nat*
818 *Rev Cancer*. 2023;23(2):57–77.

819 66. Matusiak M, et al. Spatially Segregated Macrophage Populations Predict Distinct Outcomes
820 In Colon Cancer. *Cancer Discov*. 2024;14(8):1418-1439.

67. Zhou SL, et al. Tumor-Associated Neutrophils Recruit Macrophages and T-Regulatory Cells to Promote Progression of Hepatocellular Carcinoma and Resistance to Sorafenib. *Gastroenterology*. 2016;150(7):1646-1658.e17.

68. Taïeb J, et al. Efficacy of immune checkpoint inhibitors in microsatellite unstable/mismatch repair-deficient advanced pancreatic adenocarcinoma: an AGEO European Cohort. *Eur J Cancer*. 2023;188:90–97.

69. Zong L, et al. Lipoxin A4 reverses mesenchymal phenotypes to attenuate invasion and metastasis via the inhibition of autocrine TGF-β1 signaling in pancreatic cancer. *J Exp Clin Cancer Res*. 2017;36(1):1–12.

70. Schnittert J, et al. Reprogramming tumor stroma using an endogenous lipid lipoxin A4 to treat pancreatic cancer. *Cancer Lett*. 2018;420:247–258.

Figures

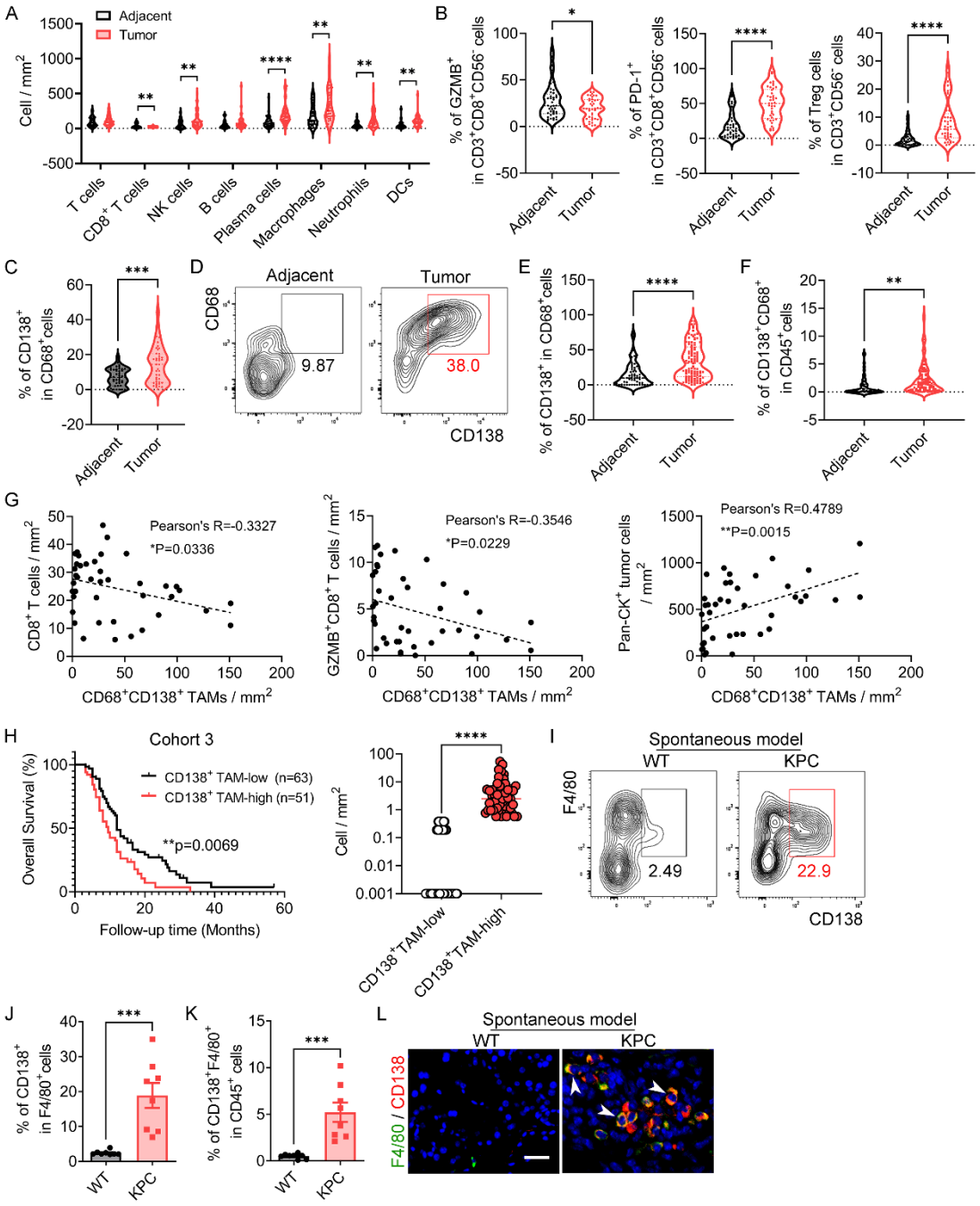

Figure 1. A CD138$^+$ TAM subpopulation is identified and associated with immune evasion and poor prognosis in PDAC. (**A-C**) Abundance of various immune cell types (**A**) and the proportions of activated cytotoxic and exhausted CD8$^+$ T cells within CD8$^+$ T cells, Treg cells among T cells (**B**), and CD138$^+$ TAMs among macrophages (**C**). The analysis utilized mIHC data

from 41 paired adjacent benign and tumor tissue samples collected from PDAC patients in Cohort 2. (**D**) Representative images of $CD138^+$ macrophages in adjacent benign (n=58) and tumor tissues (n=103) from PDAC patients in Cohort 1. (**E** and **F**) Quantification of (**D**) with graphs depicting the frequencies of $CD138^+$ macrophages in $CD68^+$ macrophages (**E**) and in $CD45^+$ cells (**F**). (**G**) Correlation among the abundance of $CD138^+$ TAMs, $CD8^+$ T cells, activated cytotoxic $CD8^+$ T cells, and Pan-CK^+ tumor cells in tumor tissues from PDAC patients in Cohort 2 (n=41). (**H**) Kaplan-Meier survival curves generated for the abundance of $CD138^+$ TAMs calculated through multispectral analysis of tumor tissues from PDAC patients in Cohort 3. This analysis categorized patients into two groups: $CD138^+$ TAM-high and $CD138^+$ TAM-low (graph on the right), revealing median survival times of 9.5 and 12 months, respectively (p-value=0.0069, HR 1.685, 95% CI 1.098 to 2.584). (**I**) Flow cytometric images of $CD138^+$ macrophages in the tumor tissues of spontaneous KPC mice. (**J** and **K**) Quantification of (**I**), representing the frequencies of $CD138^+$ macrophages in $F4/80^+$ macrophages (**J**) and in $CD45^+$ cells (**K**) (n=8 per group). (**L**) Immunofluorescence microscopy images of tumors from spontaneous KPC mice showing the presence of $CD138^+$ macrophages (white arrows). Scale bar, 10μm. *p<0.05, **p<0.01, ***p<0.001, and ****p<0.0001 by paired or unpaired t-test (**A**-**C**, **E**, **F**, **J**, and **K**), by Pearson's correlation analysis (**G**), and by log-rank analysis (**H**). Data represent mean ± SEM.

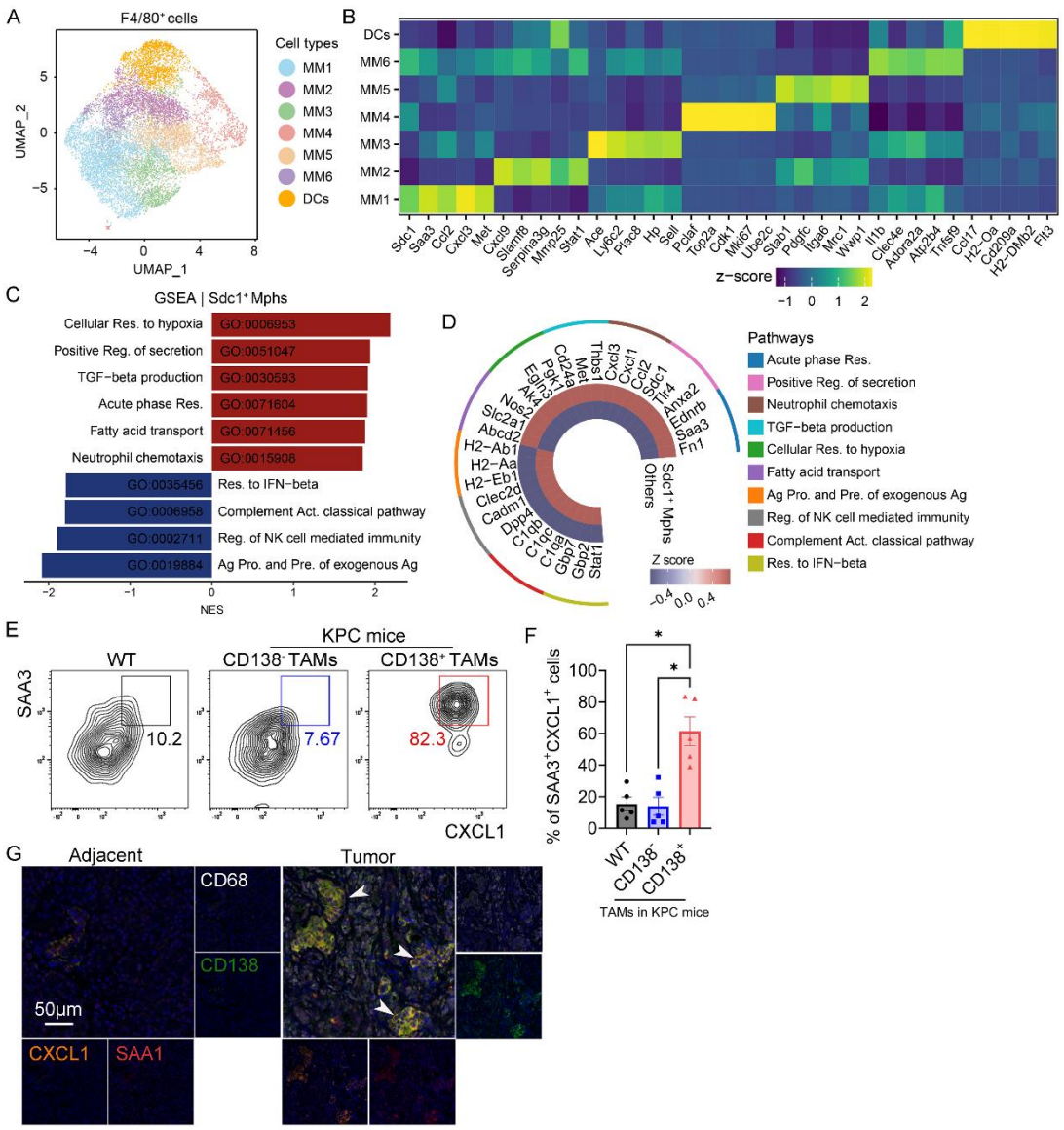

Figure 2. The CD138$^+$ TAM subset exhibits pro-inflammatory and neutrophil-chemotactic activity. (**A**) UMAP plots illustrating F4/80$^+$ cells sorted from orthotopic tumors, with colors representing distinct scRNA-seq clusters. (**B**) Heatmap displaying the scaled expression levels of marker genes across the identified macrophage and DC subsets. (**C**) GSEA of GO biological processes on genes ranked by log_2FC between *Sdc1*$^+$ TAMs and other clusters. Abbreviations include: Mphs for macrophages; Res. for response; Reg. for regulation; TGF-beta for transforming growth factor beta; Ag for antigen; Pro. for processing; Pre. for presentation; NK for natural killer;

Act. for activation; IFN-beta for Interferon Beta. (**D**) Heatmap illustrating the expression of selected genes belonging to the indicated categories as shown in (**C**), comparing *Sdc1*$^{+}$ TAMs with other subsets depicted in (**A**). (**E**) Frequencies of SAA3^{+}CXCL1^{+} cells in F4/80^{+} macrophages derived from the pancreas of wild-type mice, as well as in F4/80^{+}CD138^{-} and F4/80^{+}CD138^{+} TAMs from orthotopic KPC mice. (**F**) Quantification of (**E**) (n=5 per group). (**G**) Representative mIHC images depicting CD68^{+}CD138^{+}SAA1^{+}CXCL1^{+} TAMs (white arrows) in paired adjacent benign and tumor tissues from PDAC patients in Cohort 2. *$p<0.05$ by Kruskal-Wallis test with Dunn's multiple comparison test (**F**). Data represent mean ± SEM.

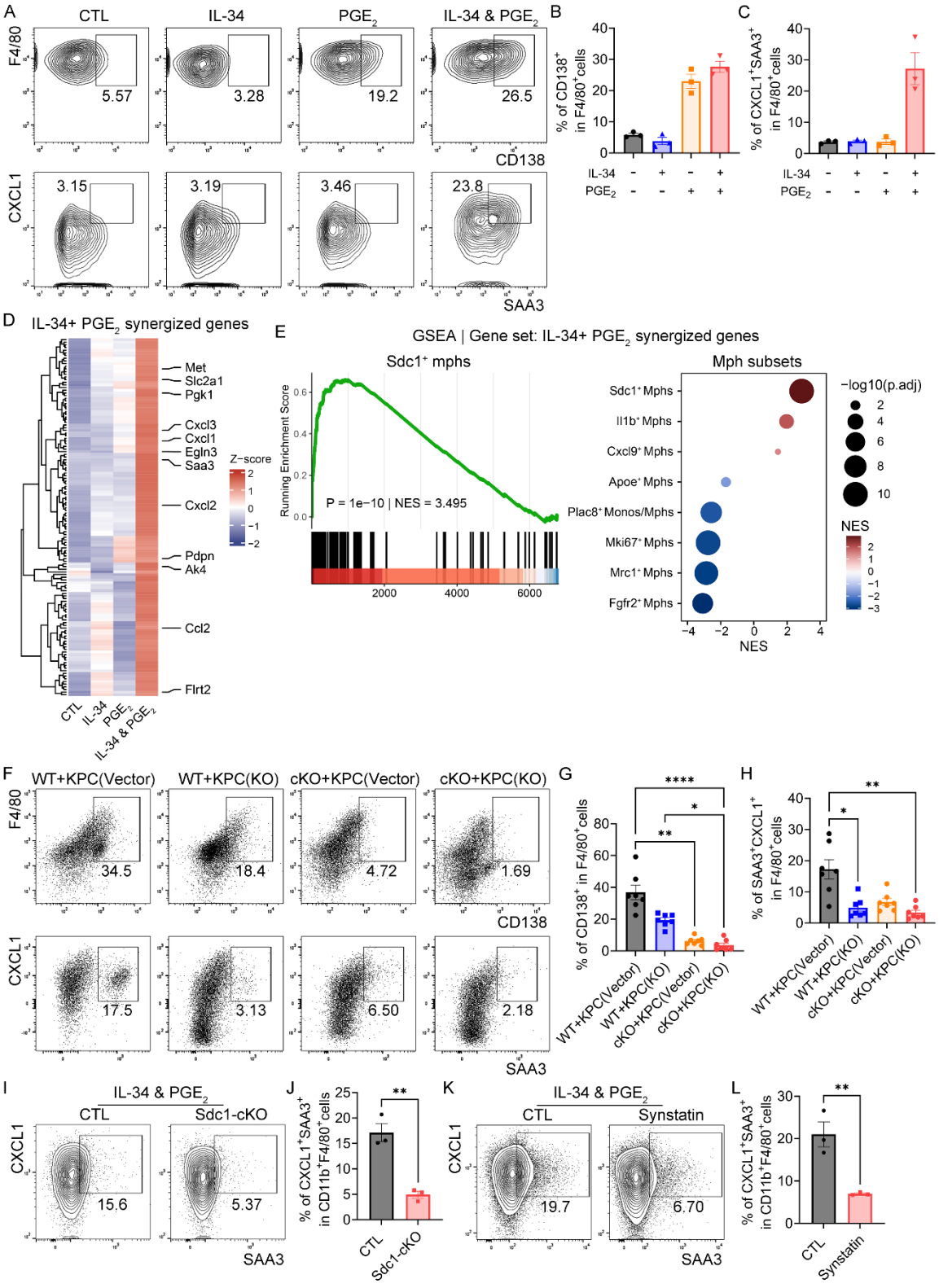

875

876 **Figure 3. The formation of CD138$^+$ TAMs is induced via IL-34-syndecan-1 and PGE$_2$-EP2**

877 **signaling.** (**A**) Representative flow cytometric images illustrating the expression levels of CD138,

878 CXCL1, and SAA3 in F4/80^{+} cells from BMDM cultures treated with IL-34 and/or PGE_2. (**B** and
879 **C**) Quantification of (**A**), showcasing the percentages of CD138^{+} (**B**) and CXCL1^{+}SAA3^{+} (**C**)
880 within F4/80^{+} population (n=3 per group). (**D**) Heatmap of the relative expression of genes
881 synergized by IL-34 plus PGE_2 in BMDM cultures. (**E**) GESA of genes synergized by IL-34 plus
882 PGE_2, on genes ranked by their correlation with the fate probability of the monocyte-to-*Sdc1*$^{+}$
883 TAM trajectory (left) and by log_2FC between each monocyte/macrophage (mono/mph) subset
884 versus other monocytes/macrophages (right). (**F**) Representative images showing the expression
885 of CD138, CXCL1, and SAA3 in F4/80^{+} cells within tumor tissues from control or Ptger2-cKO
886 mice bearing orthotopic KPC^{vector} or KPC$^{Il34\text{-}KO}$ tumors. (**G** and **H**) Quantification of (**F**),
887 illustrating the percentages of CD138^{+} (**G**) and CXCL1^{+}SAA3^{+} (**H**) within F4/80^{+} macrophages
888 (n=7 per group). (**I**) Flow cytometric images of CXCL1^{+} SAA3^{+} macrophages in the cultures of
889 BMDMs derived from control or Sdc1-cKO mice in the presence of IL-34 and PGE_2. (**J**)
890 Quantification of (**I**), showing the percentages of CXCL1^{+}SAA3^{+} within F4/80^{+} macrophages (n=3
891 per group). (**K**) Representative images of CXCL1^{+}SAA3^{+} macrophages in BMDM cultures treated
892 with IL-34 and PGE_2, with or without Synstatin, a selective inhibitor of syndecan-1. **(L**)
893 Quantification of (**K**), highlighting the percentages of CXCL1^{+}SAA3^{+} in F4/80^{+} macrophages
894 (n=3 per group). *p<0.05, **p<0.01, and ****p<0.0001 by Kruskal-Wallis test with Dunn's
895 multiple comparison test (**G** and **H**) and by unpaired t-test (**J** and **L**). Data represent mean ± SEM.
896

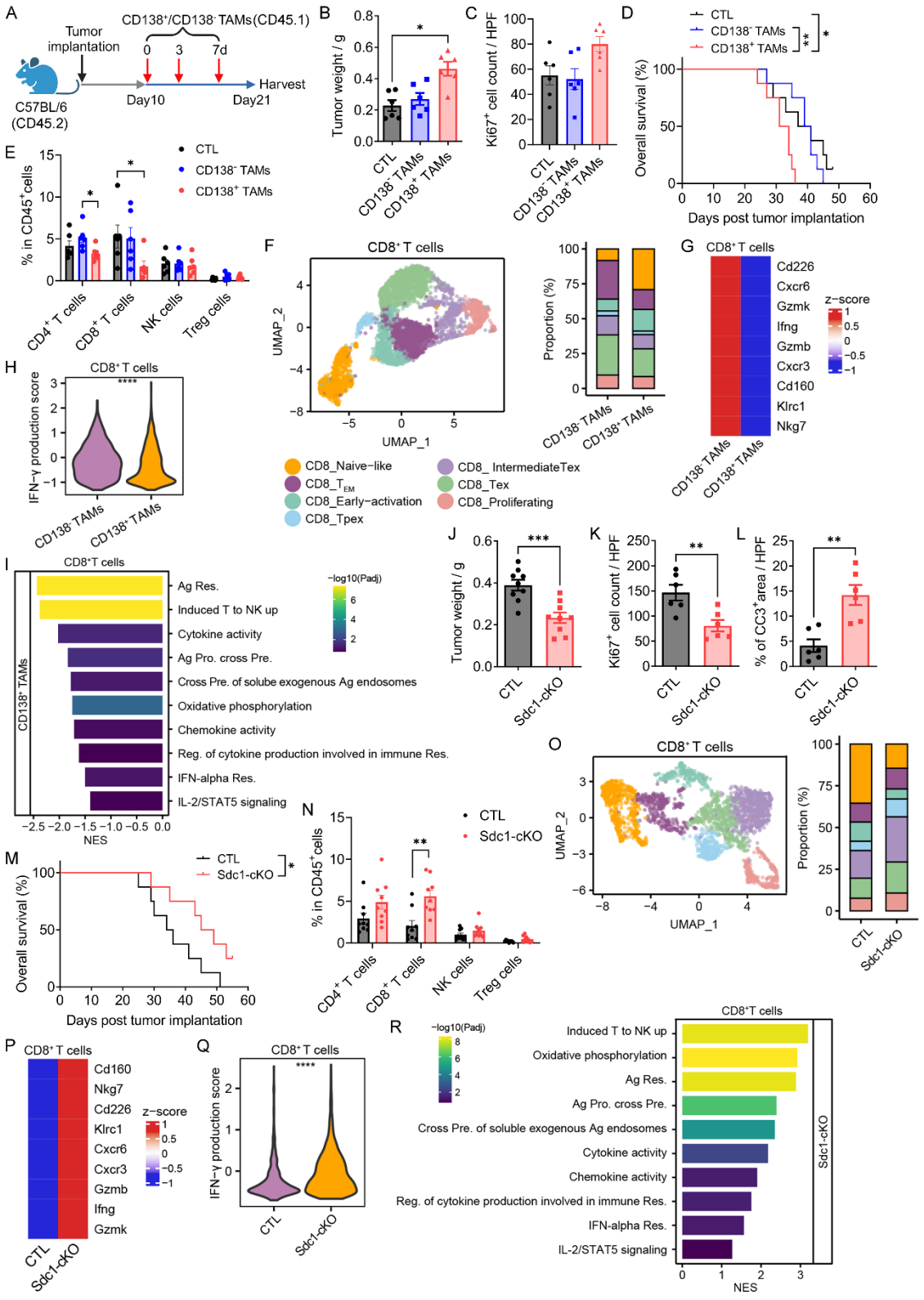

Figure 4. CD138$^+$ TAMs facilitate the progression of PDAC by promoting tumor immune evasion. (**A**) Experimental approach utilized for the adoptive transfer of CD138$^+$ or CD138$^-$ TAMs

isolated from CD45.1$^+$ orthotopic tumors into CD45.2$^+$ orthotopic KPC mice. (**B** and **C**) Quantification of tumor weight in mice (**B**) and the number of Ki67$^+$ cells per 40X field in tumor sections (**C**) (n=6 per group). (**D**) Overall survival probabilities of mice received the adoptive transfer (n=8 per group). (**E**) Quantification of the frequencies of effector cell subsets within CD45$^+$ cells in tumor tissues (n=6 per group). (**F**) Analysis of UMAP (left) and the proportions (right) of CD8$^+$ T cell clusters in tumor tissues. (**G**) Heatmap of the relative expression of effector cytokines in tumor-infiltrating CD8$^+$ T cells. (**H**) GSEA of the gene set related to IFNγ production. (**I**) GSEA of pathways associated with CD8$^+$ T cell proliferation and activation. (**J**) Quantification of tumor weight in mice (n=9 per group). (**K** and **L**) Quantification of the number of Ki67$^+$ cells (**K**) and the percentage of CC3$^+$ area (**L**) per 40X field in tumor sections (n=6 per group). CC3, cleaved caspase-3. (**M**) Overall survival probabilities of control and Sdc1-cKO mice (n=8 per group). (**N**) Quantification of the frequencies of effector cell subsets within CD45$^+$ cells in tumor tissues (n=9 per group). (**O**) Analysis of UMAP (left) and the proportions (right) of CD8$^+$ T cell clusters in tumor tissues. (**P**) Heatmap of the relative expression of effector cytokines in tumor-infiltrating CD8$^+$ T cells. (**Q**) GSEA of the gene set related to IFNγ production. (**R**) GSEA of pathways associated with CD8$^+$ T cell proliferation and activation. *p<0.05, **p<0.01, and ***p<0.001 by Kruskal-Wallis test with Dunn's multiple comparison test (**B** and **E**), by log-rank analysis (**D** and **M**), and by unpaired t-test (**J**-**L**, and **N**). Data represent mean ± SEM.

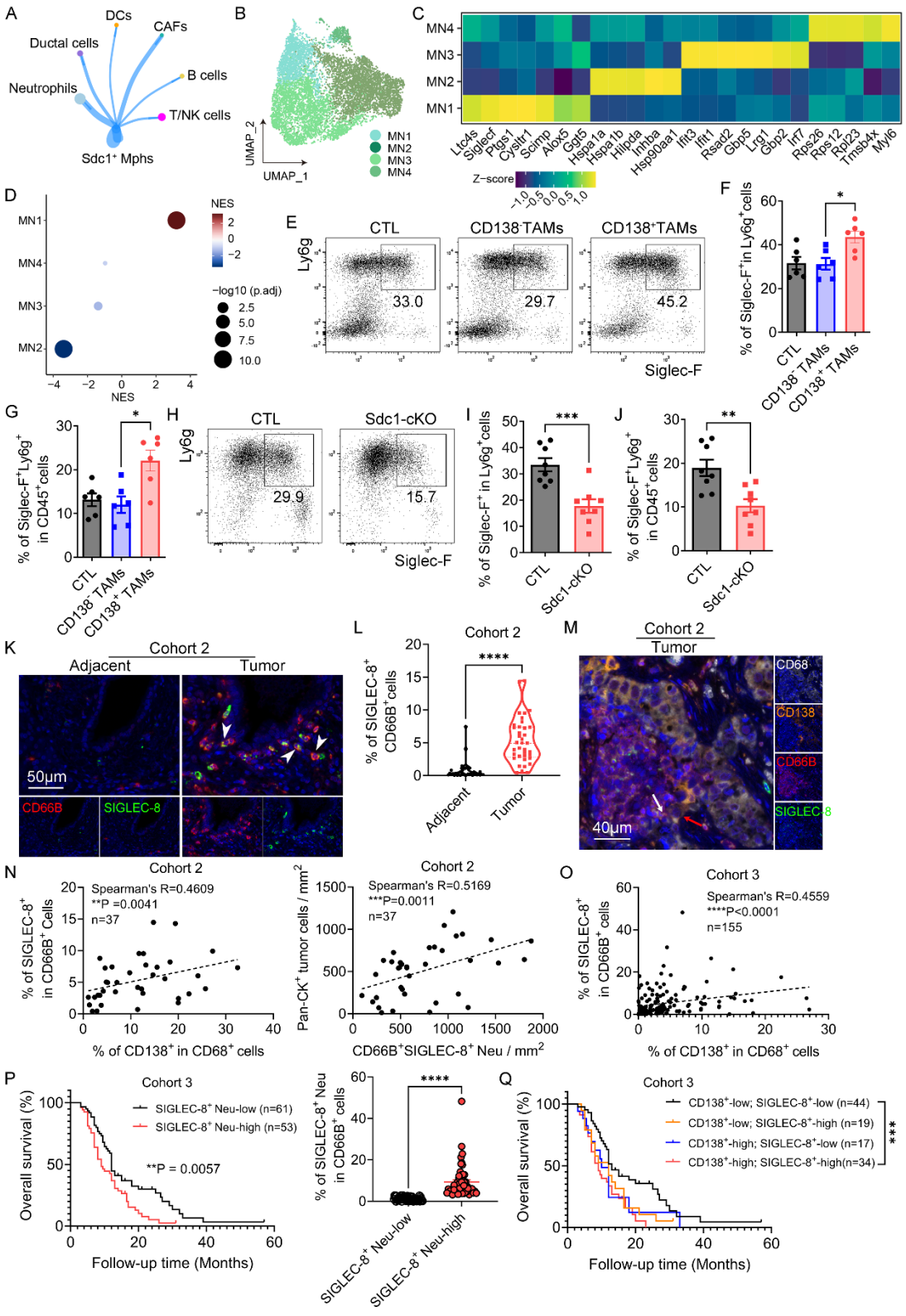

Figure 5. There exists a significant cell-to-cell interaction between CD138$^+$TAMs and Siglec-F$^+$ neutrophils in PDAC. **(A)** Cell-to-cell interactions among *Sdc1*$^+$ TAMs and other major

clusters, visualized using CellChat. (**B**) UMAP plots illustrating the reclustering of neutrophils. (**C**) Heatmap depicting the scaled expression of marker genes across neutrophil subsets. (**D**) GSEA of the gene set comprising DEGs between Siglec-F^+ and Siglec-F^- neutrophils in orthotopic tumors, based on the marker genes of neutrophil subsets. (**E**) Images depicting the presence of Siglec-F^+ neutrophils in orthotopic tumors following the adoptive transfer of $CD138^+$ TAMs. (**F** and **G**) Quantification of (**E**) (n=6 per group). (**H**) Images displaying Siglec-F^+ neutrophils in the orthotopic tumors of Sdc1-cKO mice. (**I** and **J**) Quantification of (**H**) (n=8 per group). (**K**) Images showing SIGLEC-8^+ neutrophils (white arrows) in PDAC patients. (**L**) Quantification of (**K**) (n=37-38 per group). (**M**) Images revealing the co-localization of $CD138^+$ TAMs (red arrow) with SIGLEC-8^+ neutrophils (white arrow) in PDAC patients. (**N** and **O**) The correlation among SIGLEC-8^+ neutrophils, $CD138^+$ TAMs, and Pan-CK^+ tumor cells in PDAC patients. (**P**) Kaplan-Meier survival curves generated based on the frequencies of SIGLEC-8^+ neutrophils. The curves reveal a median survival of 9.0 months for the SIGLEC-8^+ Neu-high group compared to 12 months for the SIGLEC-8^+ Neu-low group (p-value = 0.0057, HR 1.860, 95% CI 1.198 to 2.888). (**Q**) Kaplan-Meier survival curves generated for $CD138^+$ TAM abundance and SIGLEC-8^+ neutrophil frequency. Comparison between $CD138^+$-high, SIGLEC-8^+-high and $CD138^+$-low, SIGLEC-8^+-low groups yields a median survival of 9.0 vs. 13.0 months (p-value = 0.0010, HR 2.635, 95% CI 1.482 to 4.687). *p<0.05, **p<0.01, ***p<0.001, and ****p<0.0001 by Kruskal-Wallis test with Dunn's multiple comparison test (**F** and **G**), by paired or unpaired t-test (**I**, **J**, and **L**), by Spearman's correlation analysis (**N** and **O**), and by log-rank analysis (**P** and **Q**). Data represent mean ± SEM.

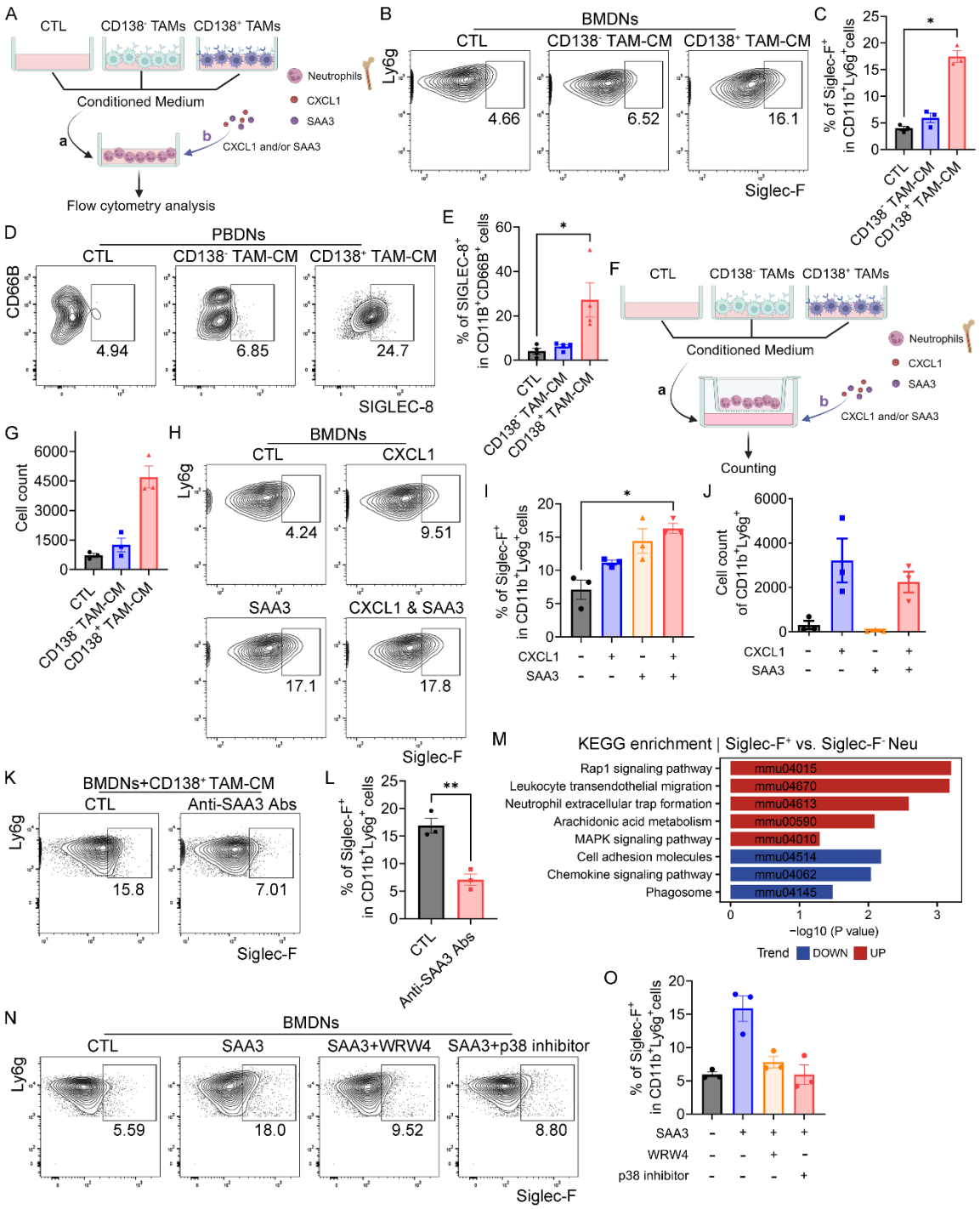

Figure 6. CD138⁺ TAMs promote the polarization and migration of Siglec-F⁺ neutrophils through the actions of SAA3 and CXCL1. (**A**) Schematic diagram illustrating the culture of BMDNs treated with CM derived from CD138⁺ or CD138⁻ TAMs isolated from orthotopic tumors, as well as with SAA3 and/or CXCL1. (**B** and **H**) Representative images depicting the frequencies

of Siglec-F^+ in $Ly6g^+$ neutrophils in BMDN cultures upon treatment with CM (**B**) or CXCL1 and/or SAA3 (**H**). (**C**) Quantification of (**B**) (n=3 per group). (**D**) Images revealing the percentages of SIGLEC-8^+ in $CD66B^+$ neutrophils in human PBDN cultures exposed to CM derived from $CD138^+$ or $CD138^-$ TAMs in PDAC patients. (**E**) Quantification of (**D**) (n=4 per group). (**F**) Experimental approach to evaluate the cell migration capacity of BMDNs through a transwell culture system exposed to CM derived from $CD138^+$ or $CD138^-$ TAMs isolated from orthotopic tumors, as well as to SAA3 and/or CXCL1. (**G** and **J**) Quantification of the number of migrated cells in the transwell culture system exposed to CM (**G**) or CXCL1 and/or SAA3 (**J**) (n=3 per group). (**I**) Quantification of (**H**) (n=3 per group). (**K**) Representative images depicting the frequencies of Siglec-F^+ in $Ly6g^+$ neutrophils in BMDN cultures exposed to $CD138^+$ TAM-CM with or without anti-SAA3 neutralizing antibodies. (**L**) Quantification of (**K**) (n=3 per group). (**M**) KEGG enrichment analysis of DEGs between Siglec-F^+ and Siglec-F^- neutrophils derived from orthotopic tumors. (**N**) Images displaying the frequencies of Siglec-F^+ in $Ly6g^+$ neutrophils in BMDN cultures exposed to SAA3 with or without WRW4 (a FPR2 antagonist) or p38 MAPK-IN-1 (a p38 MAPK pathway inhibitor). (**O**) Quantification of (**N**) (n=3 per group). *$p<0.05$ and **$p<0.01$ by Kruskal-Wallis test with Dunn's multiple comparison test (**C**, **E**, and **I**) and by unpaired t-test (**L**). Data represent mean ± SEM.

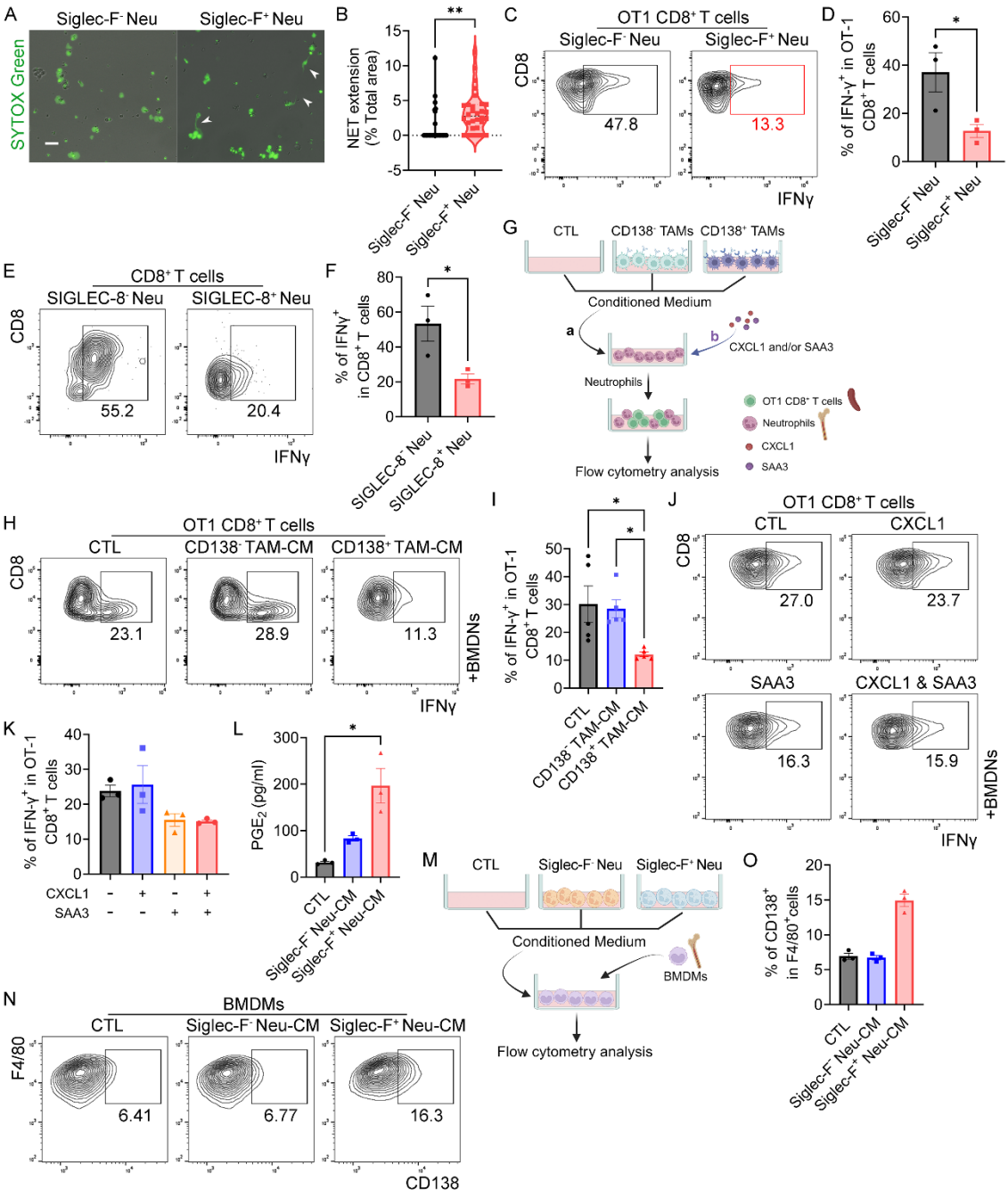

Figure 7. A feedforward loop between CD138$^+$ TAMs and Siglec-F$^+$ neutrophils drives tumor immune evasion by inhibiting the anti-tumor effects of CD8$^+$ T cells. (**A**) Representative images showing NET formation (white arrows) in Siglec-F$^+$ and Siglec-F$^-$ neutrophils isolated from orthotopic tumors. Scale bar, 20μm. (**B**) Quantification of (**A**) by calculating the percentage of the total area covered by the SYTOX Green–positive region (n=30 per group). (**C**) Plots depicting

IFNγ production by OT1 $CD8^+$ T cells from co-cultures of splenocytes from OT1 transgenic mice with either Siglec-F^- or Siglec-F^+ neutrophils sorted from orthotopic tumors. (**D**) Quantification of (**C**) (n=3 per group). (**E**) Images depicting IFNγ production by activated $CD8^+$ T cells from co-cultures involving $CD8^+$ T cells derived from human peripheral blood and either tumor-infiltrating SIGLEC-8^- or SIGLEC-8^+ neutrophils in patients with PDAC. (**F**) Quantification of (**E**) (n=3 per group). (**G**) Schematic diagram illustrating the co-cultures of splenocytes isolated from OT1 transgenic mice with BMDNs treated with CM derived from $CD138^+$ or $CD138^-$ TAMs sorted from orthotopic tumors, as well as with CXCL1 and/or SAA3. (**H** and **J**) Plots displaying IFNγ production by OT1 $CD8^+$ T cells from the indicated co-culture groups upon treatment with CM (**H**) or CXCL1 and/or SAA3 (**J**). (**I**) Quantification of (**H**) (n=5 per group). (**K**) Quantification of (**J**) (n=3 per group). (**L**) Quantification of PGE_2 levels in CM derived from Siglec-F^- and Siglec-F^+ neutrophils sorted from orthotopic tumors (n=3 per group). (**M**) Schematic diagram illustrating the cultures of BMDMs upon treatment with CM derived from Siglec-F^+ or Siglec-F^- neutrophils sorted from orthotopic tumors. (**N**) Images showing the percentages of $CD138^+$ macrophages in BMDM cultures treated with CM. (**O**) Quantification of (**N**) (n=3 per group). *$p<0.05$ and **$p<0.01$ by unpaired t-test (**B**, **D**, and **F**) and by Kruskal-Wallis test with Dunn's multiple comparison test (**I** and **L**). Data represent mean ± SEM.

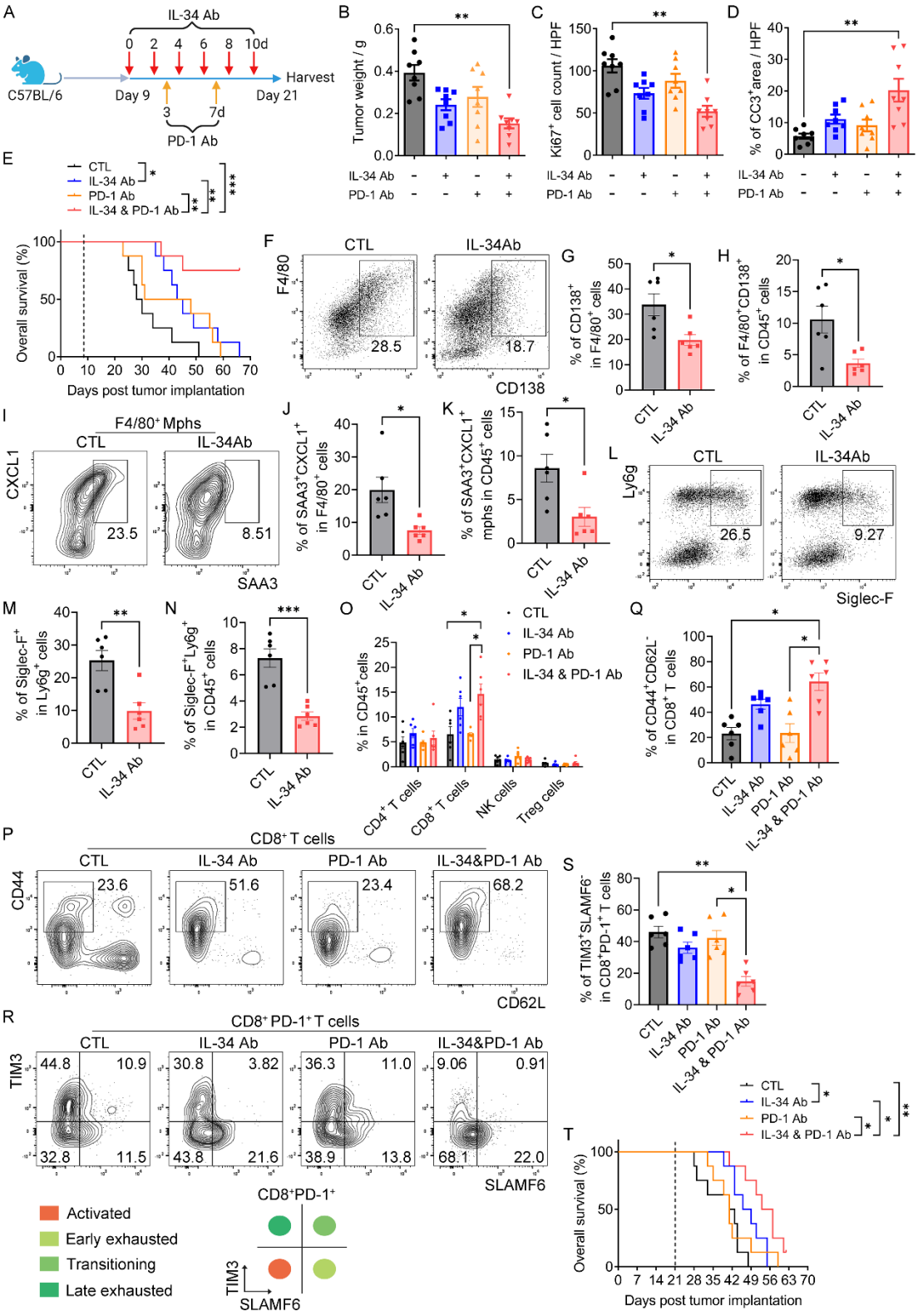

Figure 8. Anti-IL-34 antibodies abrogate tumor progression and enhance responses to anti-PD-1 immunotherapy in PDAC by disrupting the CD138$^+$ TAM-Siglec-F$^+$ neutrophil axis. (A)

Experimental design employed to evaluate the therapeutic efficacy of anti-IL-34 antibodies in conjunction with anti-PD-1 antibodies in PDAC. (**B**) Quantification of tumor weight (n=8 per group). (**C** and **D**) Quantification of $Ki67^+$ cell counts (**C**) and the percentage of $CC3^+$ area (**D**) per 40X field in tumor sections (n=8 per group). (**E**) Overall survival probabilities of mice (n=8 per group). The dashed line indicates the timepoint when the combination therapy commenced. (**F** and **I**) Flow cytometric images showing $CD138^+F4/80^+$ (**F**) and $SAA3^+CXCL1^+$ (**I**) macrophages in the tumor tissues of mice following anti-IL-34 antibody treatment. (**G** and **H**) Quantification of (**F**) (n=6 per group). (**J** and **K**) Quantification of (**I**) (n=6 per group). (**L**) Representative plots illustrating the presence of Siglec-F^+ neutrophils in the tumor tissues of mice upon treatment with anti-IL-34 antibodies. (**M** and **N**) Quantification of (**L**) (n=6 per group). (**O**) Quantification of the frequencies of effector cell subsets among $CD45^+$ cells in the tumor tissues (n=6 per group). (**P** and **R**) Representative images depicting $CD44^+CD62L^-$ effector (**P**) and $TIM3^+SLAMF6^-PD\text{-}1^+$ late-exhausted (**R**) $CD8^+$ T cells within the tumor tissues. (**Q**) Quantification of (**P**) (n=6 per group). (**S**) Quantification of (**R**) (n=6 per group). (**T**) Overall survival probabilities of mice (n=8 per group). The dashed line indicates the timepoint when the combination therapy commenced. *p<0.05, **p<0.01, and ***p<0.001 by Kruskal-Wallis test with Dunn's multiple comparison test (**B**-**D**, **O**, **Q**, and **S**), by log-rank analysis (**E** and **T**), and by unpaired t-test (**G**, **H**, **J**, **K**, **M**, and **N**). Data represent mean ± SEM.